Optical Spectroscopy on High-Temperature Superconductors

OPTICAL SPECTROSCOPY ON HIGH-TEMPERATURE SUPERCONDUCTORS

By
GREG EGAN, B. Sc.

A Thesis

Submitted to the School of Graduate Studies in partial fulfillment of the

Requirements for the Degree of

Masters of Science

McMaster University

MASTER'S OF SCIENCE (2010)	**McMaster University**
(Physics and Astronomy)	**Hamilton, Ontario**

TITLE:	**Optical Spectroscopy on High-Temperature Superconductors**
AUTHOR:	**Greg Egan** **B. Sc., 2008 (University of Waterloo, Ontario)**
SUPERVISOR:	**Professor T. Timusk**
NUMBER OF PAGES:	i-x, 67

Abstract

Optical spectroscopy is an experimental tool used to probe the intermediate-energy level excitations in solid materials with the ultimate goal of achieving a bosonic spectral function. Reflectance of a sample is measured and then manipulated to yield frequency-dependent conductivity, dielectric functions, scattering rates and self-energies. The technique is particularly useful in probing the underlying electronic mechanisms in high-temperature superconductors.

The technique is applied to an iron pnictide superconductor, namely $BaFe_{1.8}Co_{0.2}As_2$. The reflectance is measured and reported, along with all relevant quantities derived from this result. In particular the bosonic spectral function is uncovered and then interpreted.

In addition, a "proof of concept" is included to illustrate the advantages and disadvantages of the Maximum Entropy Inversion method which is used to uncover the boson spectral function. The results reported here make reference to an already published article on the Bi-2212 superconductor and the conclusion will be verified.

Acknowledgements

Foremost, I would like to acknowledge the guidance and support of my supervisor, Prof. Tom Timusk PhD. I would also like to thanks Prof. Jules Carbotte PhD for his contributions to the theoretical formulation of our study. Additionally, I would like to thank my coworkers, Sarah Purdy, Jesse Hall, and Allison Kinross for all of their technical assistance with this project. Former students, Jungseek Hwang and Jing Yang have also been instrumental to the continual progress on the project. Special thanks to Paul Dube for providing us with liquid helium as well as with troubleshooting assistance in the lab. Lastly, but certainly not least, I'd like to express my extreme gratitude towards my family. Over the past years, I've been blessed by their unwavering and overwhelming emotional, intellectual, and financial support, for which I am eternally grateful.

Contents

List of Figures

List of Tables

1 .Introduction

This thesis will focus primarily on the technique of optical spectroscopy and the insights it can gain on the pairing mechanism of unconventional superconductors with special attention paid to advances to the instrumentation. In particular, results will be displayed for the iron pnictide superconductor $BaFe_{1.8}Co_{0.2}As_2$. An overview of the Maximum Entropy Inversion for uncovering the bosonic spectral function is also provided with reference to a previously published paper on the Bi-2212 superconductor.

1.1 Intro to Optical spectroscopy

Optical spectroscopy is an investigative tool used on numerous systems to probe the interaction of the electronic structure with the incident energy and thus gain insight on the transport properties. The technique used here covers a very large spectral region ranging from the FIR (~50 cm^{-1}) up to the UV region (40,000 cm^{-1}) using a commercially available Bruker IFS 66v/S spectrometer. The FIR region is of particular importance in the study of superconductivity and other interactions that occur in the low energy regime. Figure 1 is an illustration highlighting some of the electronic interactions available (Basov and Timusk, 2005).

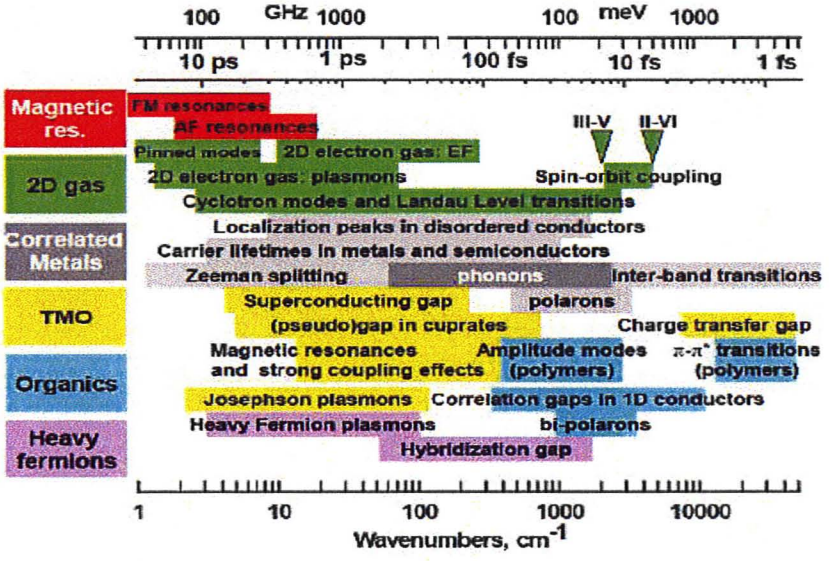

Figure 1: Illustration of intermediate energy excitations

Although other techniques exist in the study of electronic transport properties, optical spectroscopy has a few key advantages which have been exploited here. One of the most obvious benefits is sufficiently accurate data can be gathered on samples with surface area down to the hundreds of micrometer scale. This is particularly important when studying materials in rapidly evolving fields like superconductivity where reliable growths of large samples are not always an available luxury. For example, magnetic neutron scattering requires bulkier samples due to the weak interaction of the probing neutrons. As well, the penetration depth of the optical radiation is on the hundreds of

nanometer scale and consequently any sample or film thicker than this scale will be sufficient. The optical spectroscopy technique described in this thesis is a popular and attractive tool for the study of low-lying electronic excitations in exotic materials.

1.2 Introduction to Iron Arsenide Superconductors

Superconductivity has been on the forefront of scientific research since it was first reported. The phenomenon was first observed in the Hg in 1911 (Onnes, 1911) and has since expanded to a large collection of compounds. On the macroscopic scale, superconductivity can be characterized by perfect diamagnetism and zero resistivity. Perfect diamagnetism is the complete expulsion of magnetic fields in a bulk material while zero resistivity is simply the absence of current depletion through the material. On the microscopic scale, a gap in the density of states opens at the Fermi surface. All of these behaviors were described by the Bardeen-Cooper-Schriefer theory in 1957 which assigns an order parameter to the superconducting state (Bardeen et al., 1957). In this semi-classical model, free electrons are allowed to interact with the surrounding lattice of positive ions. As the free electron passes through the lattice, the positive ions are pulled inwards from the Coulomb interaction. The time scale for the movement of the ions is much longer than the fast-moving conducting electron which results in a small region of space with a total net positive charge being created. This net positive charge is seen by a second electron and causes an attraction. In essence, the first electron is "paired" with the second electron creating what is known as a Cooper pair. This description is called an

electron-phonon interaction.

Although this simple model was adequate for early superconductors, it failed as more families of materials were discovered to exhibit the behavior. In 1968, Bednorz and Mueller discovered a class of superconductors in copper oxide (cuprate) type materials which came to be known as the High-Temperature Superconductors (HTSC) for their unexpectedly high transition temperatures ranging from 30 K to 135 K (Bednorz and Mueller, 1986). The cuprates contain alternating conductive layers of CuO planes separated but insulating layers. These superconductors display variable critical transition temperatures with variation in carrier doping, this behavior is unique to the HTSCs. As oxygen is added to the system, the dopant provides holes to the system and the superconducting phase starts at a critical doping level. The transition temperature rises with increased doping until reaching a maximum temperature, signifying an optimally doped system. Beyond this optimal doping, the transition temperature begins to fall again. Typically, the relationship between doping and transition temperature forms a dome-like shape. This simple picture is further complicated when considering the normal states outside of the superconducting dome. Simple metals display a Fermi-liquid behavior (Kittell, 1976), while the cuprates exhibit a variety of unique characteristics. Below a certain characteristic temperature, T^*, the normal state shows a gap structure, referred to as the pseudogap. The size of the pseudogap decreases with hole doping level until it disappears entirely at optimal doping. The uniqueness of the HTSCs indicates that the simple electron-phonon interaction does not adequately describe the behavior, and

questions are raised as to whether or not other interactions, such as electron-magnon, are responsible for the superconductivity.

Another more recently discovered family of HTSCs are the iron pnictide superconductors, which contain alternating layers of charge carrying FeAs layers which can be doped to contain conducting electrons. A simple diagram of the pnictide crystal structure is illustrated in Figure 2, highlighting the alternating layer pattern. Doped compounds of LaOFeAs were discovered to exhibit superconductivity at $T_c = 26$ K in 2008 in Japan. The geometry of alternating conducting planes, along with the strong dependence on doping suggests an intrinsic link between the pairing mechanism of the cuprates and that of the pnictides. In addition to initial observations, the cuprates and pnictides share the characteristic antiferromagnetic order at low doping, and it is only after the antiferromagnetism is suppressed by increased doping that superconductivity can be observed. These simple observations suggest that information gained on the pnictides could be directly analogous to questions regarding the cuprates.

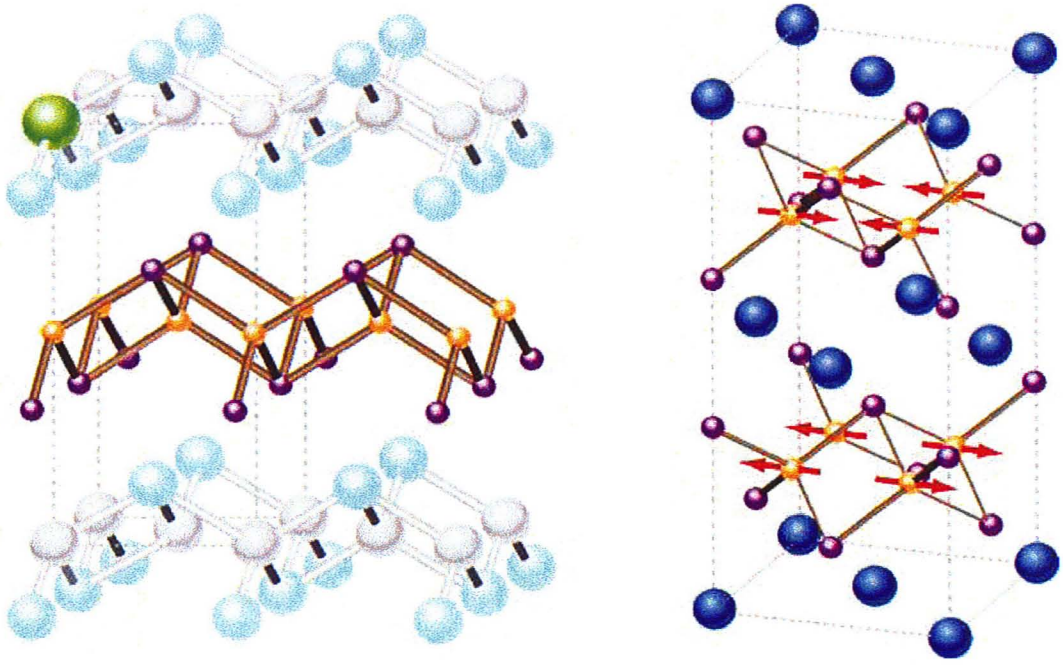

Figure 2: Iron Arsenide Structure, showing the alternating layer pattern

2. Experimental Apparatus

2.1 Bruker IFS 66/v

The experiment is done with the assistance of a commercially available Bruker IFS/66v spectrometer. The Bruker apparatus utilizes a Michelson-type interferometer. In reference to the labels on Figure 3, a beam of collimated light produced at the source ('A') is split into two using a beam splitter ('F') and sent through perpendicular paths, and then reflected back through the beam splitter and allowed to recombine. One of the light paths stays fixed ('E'), while the other is allowed to expand or contract ('H'). Path length differences in the two light paths create an interference pattern when they recombine.

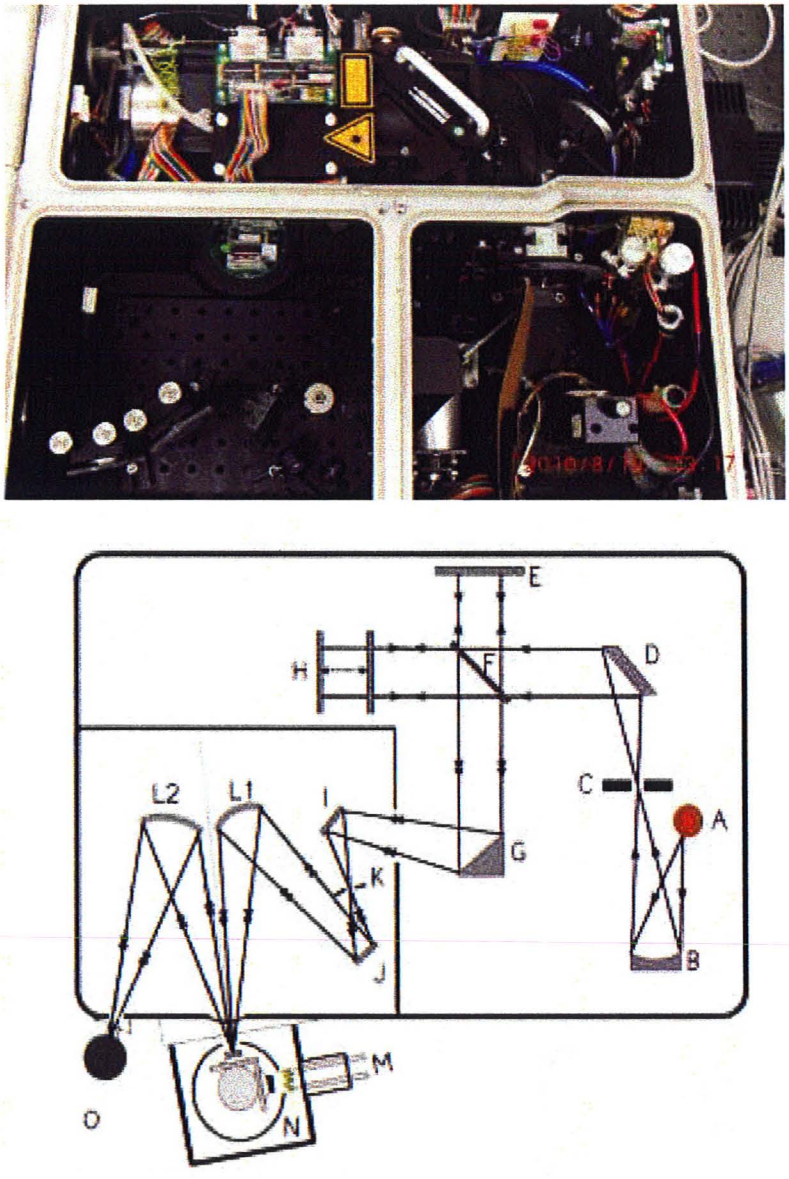

Figure 3: A top view of the inside of Bruker spectrometer (top), and the corresponding ray diagram (bottom)

This interference pattern is denoted as an "interferogram". For a simple monochromatic source, the interference pattern is a sinusoid. For more continuous light sources, the interferogram pattern is a superposition of a series of sinusoids, each corresponding to a different frequency of the source. In the Bruker, the interferogram is created and sent through a series of optics and allowed to illuminate the sample by means of an incident focusing mirror ('L1'). The reflected interferogram is then collected on a second mirror ('L2'), and focused onto the detector ('O'). The interferogram is then interpreted by computer software (OPUS) by means of a Fourier transform which converts the mirror position axis into a frequency domain. The transformed interferogram is called the spectrum and is a direct result of the frequency-dependent intensity of the light source used. Quantitatively, if the detector sees an intensity as a function of position, *W(x),* then the Fourier transformed spectrum as a function of frequency, *G(k)*, would have the form,

$$G(k) = \frac{1}{\sqrt{2\pi}} \int_{-\infty}^{\infty} W(x) e^{-ikx} dx$$

This process can be seen visually in Figure 4.

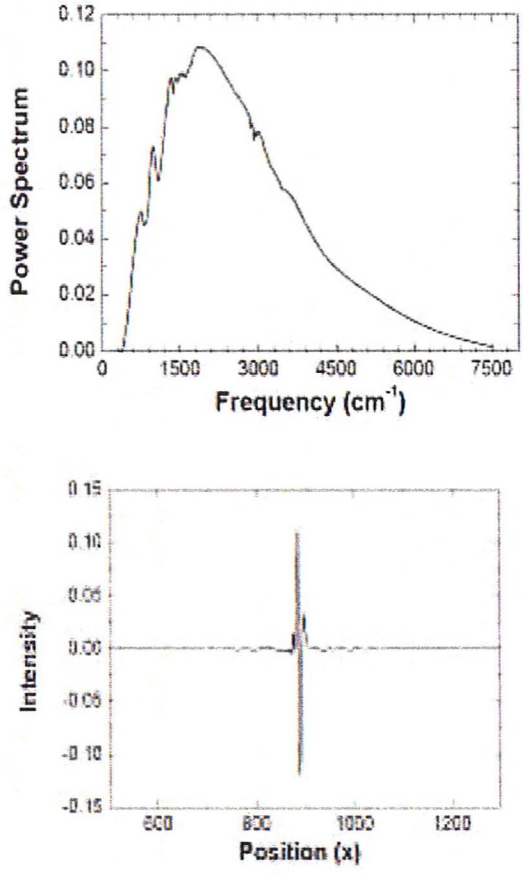

Figure 4: Illustration of the Fourier Transform method, with interferogram (top) and transformed spectrum (bottom)

Shown on the top is what is measured by the detector and on the bottom is the transformed power spectrum which matches the spectrum of the light source (MIR shown here).

2.1.1 Optical Configuration

To gain a maximum amount of information over as large a spectral region as possible, various combinations of light sources, beam splitters, and detectors are used. The following table summarizes the combinations required for each spectral region.

Spectral Region	Frequency band	Detector	Beam splitter	Window
FIR	40-250 cm^{-1}	1 K Bolometer	-6 micron Mylar (with Ge coating) -50 micron Mylar	Polypropylene
FIR	50-650 cm^{-1}	4 K Bolometer	-6 micron Mylar (with Ge coating) -50 micron Mylar	Polypropylene
MIR	400-6,000 cm^{-1}	77 K MCT	KBr	KBr
NIR	3,000-14,000 cm^{-1}	77 K MCT	CaF_2 (UV)	KBr
UV	12,000-45,000 cm^{-1}	PMT	CaF_2 (UV)	KBr

Table 1: Configuration of beam splitters/windows/detectors for the various spectral regions

A semiconductor alloy of mercury cadmium tellurium is used in the MCT detector. This style of detector is used extensively in the industry for infrared detection. The detector itself is composed of a thin layer (10-20 um) of HgCdTe with metallic contact pads defining the detection area. Photons with energy greater than the semiconductor band gap energy excite electrons into the conduction band, thereby changing the conductivity of the alloy. Since the size of the band gap is dependent on the alloy composition, the region of sensitivity can be tuned by changing the concentration of cadmium. The MCT requires cooling to function so it is kept at 77 K by means of a liquid nitrogen chamber inside the detector. The detector used here is designed to cover the spectral region from 400 to 14,000 cm^{-1}.

Figure 5: MCT detector used for the MIR and NIR regions

The bolometers (both the 1 K and 4 K) function on the principle that incident radiation will cause a small temperature fluctuation when it comes in contact with a crystal surface. The incident photon deposits its energy in the crystal surface, which is attached to a heat sink. When low energy radiation comes into contact with the crystal surface, the temperature is raised slightly and the difference between the temperature of the heat sink and the metal plate is measured. The temperature difference is proportional to the intensity and frequency of the light used, and therefore functions as an infrared detector. Our laboratory uses two bolometers that contain heat sinks at 1 K and 4 K. Understandably, the 1 K bolometer is more sensitive to lower energies as smaller temperature fluctuations can be detected. Both detectors require a cooling regiment of

liquid Helium, although the 1 K bolometer requires an extra step of pumping on the helium bath to achieve the lower temperature.

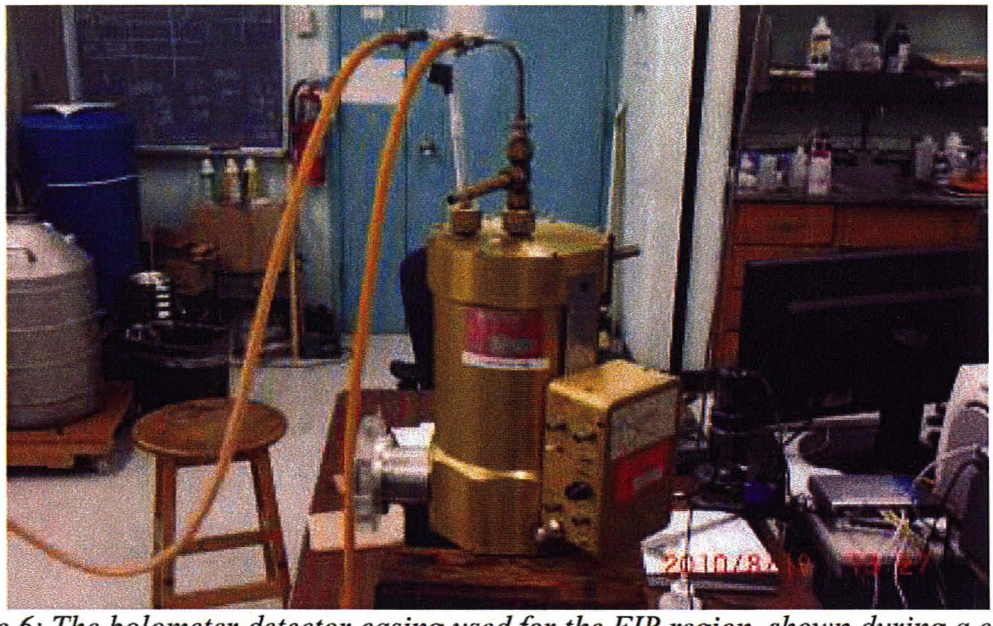

Figure 6: The bolometer detector casing used for the FIR region, shown during a coolant transfer

For the UV region, a photomultiplier tube is used. The photomultiplier tube (or PMT) is based on combination of the photoelectric effect and the principle of secondary emission, where an electron causes the emission of other electrons when incident on an electrode. The PMT contains inside a vacuum tube that houses a series of electrodes. When an incident photon strikes a photocathode, electrons are ejected according to the photoelectric effect. The ejected electron is then funneled through a series of electrodes that essentially amplifies the strength through the secondary emission effect. As the ejected electron moves through the detector it is accelerated by an applied electric field, thereby magnifying its inherent energy. After a series of amplification cathodes, the

accelerated electrons finally strike the anode at the rear of the tube, and the current is detected. PMT detectors are most suitable for larger energy photons, and are therefore used exclusively for the UV region.

Figure 7: PMT tube used in the laboratory for the UV region

2.2 A discussion of the previous setup

As described previously, the production of reflectance measurements requires the use of a stainless steel reference to account for surface geometry. The reference needs to be measured with the sample at each temperature. Since there is only one optical path, the steel reference and the sample under study need to be moved back and forth from the light source with as much reproducibility as possible.

Previous students (Jungseek Hwang PhD, Jing Yang PhD) accomplished this task

by developing a rotating sample mount with the reference and sample mounted perpendicular to each other. However, this adaptation came at the expense of temperature controlling which requires the sample to be as close as possible to the cooling cryostat. It was not feasible however to have the cryostat rotate with the sample mount in unison. To overcome this, a flexible copper braid bridged the small gap between the cryostat and the sample mount. However, the finite distance (~2.5 cm) and relatively small surface area leads to loss in thermal conduction. On top of this, the rotating sample mount is thermally grounded in that it is in contact with the bottom of the chamber and thus in contact with room temperature. This effect was minimized by use of quarts rods and nylon screw to secure the sample mount, but this is also not ideal. The copper braid along with the thermal grounding resulted in a lowest achievable temperature of approximately 25 K, which prohibited the study of phase states below this temperature. Additionally, the sample mount was limited to a single sample and the accompanying reference.

2.3 New setup

2.3.1 Light Overfilling

For any sample growth, even of the highest quality, there are bound to be small variations across the surface. Common examples include small amounts of tin flux leftover from the growth, or tiny cracks or divots in the surface. In this way, a beam of light focused sharply on a specific point on the surface may yield a different reflection than another point on the same sample. To account for this, the incident light is focused to

a spot of diameter larger than that of the sample so that the whole surface is probed on each measurement, called "light overfilling". This technique has been pioneered by Chris Holmes, and has since become very popular within optics groups. Naturally, the light that misses the sample is not relevant to the material properties so it must be scattered away from the detector. To achieve this, the samples are mounted on small brass cones which are polished to scatter light out of the optical path. A series of 6 holes (1-64, 2-56, and 1-72) are cut to assist in the alignment process, described in section 2.3.4. The brass cones are machined from stock brass material with the use of a miniature lathe and mill, found in the laboratory.

Figure 8: A picture of the brass cone. The polished conical face is designed to reflect light that misses the sample away from the detection path.

2.3.2 Sample Mount

With the objective of improving the achievable temperatures, a new design was conceived featuring a copper rod attached directly to the bottom of the cryostat to which the sample and reference can be mounted. The copper mount is in direct thermal contact with the copper "cold contact" of the cryostat and utilizes a large surface area to increase conduction. The mount was machined in the Engineering Machine Shop at McMaster and was made out of HFHC copper to maximize thermal conduction. The piece is fitted with threaded holes for mounting the samples and thermometry. The copper piece is known to tarnish, so regular polishing is required. Attached to the sample mount is thin piece of brass with charcoal epoxied on top. This charcoal works as a water trap and helps us to limit the amount of moisture inside the sample chamber. The charcoal has been demonstrated to lower the effect of ice absorption at low temperatures.

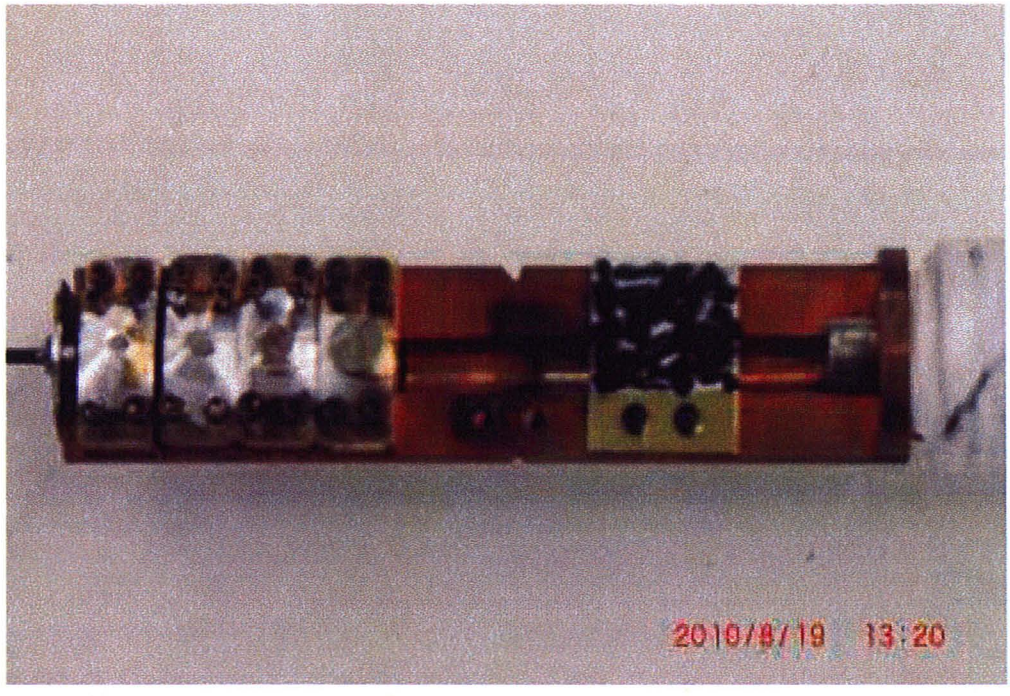

Figure 9: The copper sample mount, with cones mounted. The charcoal water trap is seen on the right.

2.3.3 Translation Stage

In order to allow the movement between sample and reference, a vertically translating stepper motor is attached outside of the sample chamber. The stepper motor controls the operation of a sturdy 3-axis bellows system constructed by McAllister Technical Services. In conjunction, the motor and bellows allow for the vertical translation of up to 3 inches of both the cryostat and the copper sample mount. The considerably large translation distance gives us the flexibility to mount a total of 4 sample cones (one being the reference). This allows us to perform measurements on three different materials in unison, a very distinct advantage over the previous design.

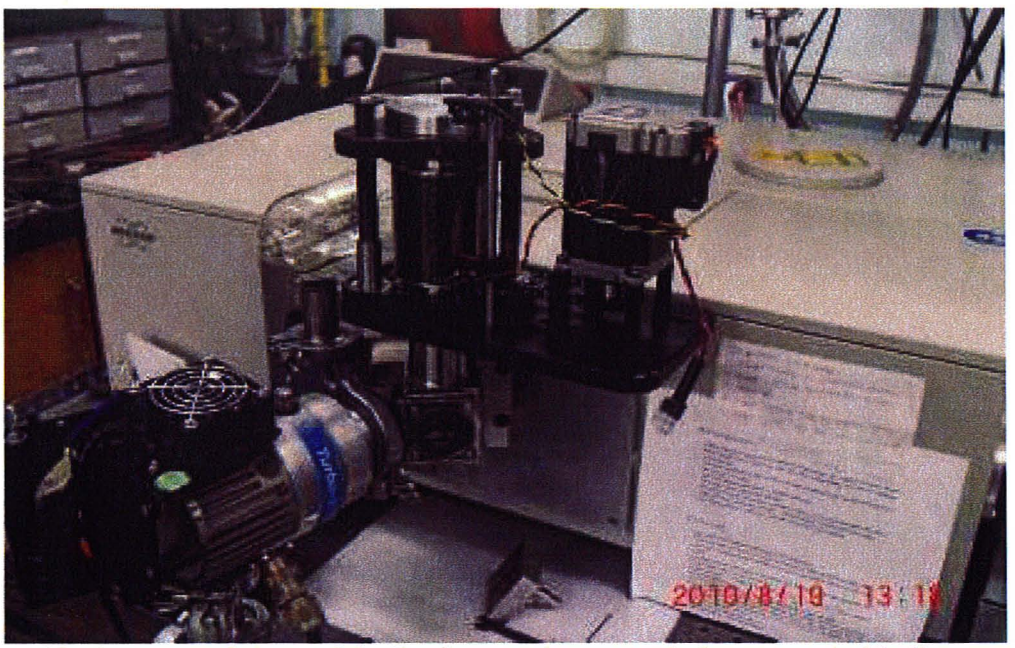

Figure 10: An external view of the Bruker apparatus with the motor and bellows system mounted

2.3.4 Optical optimization

The optimization of the optical signal is an important aspect in both the quality and the reproducibility of the data. It has been found that poor optical alignment introduces a large amount of error in the transition between temperatures. The samples are mounted in succession and the whole cryostat is placed horizontally on a mount with a sliding axis (shown in Figure 11). A laser pointer is mounted at the same height as the samples and the spot reflection of the laser off the sample is marked on a sheet of paper. This device is used for the external alignment of the samples to each other. Typically, the reference mirror is not changed from sample to sample and therefore all new samples are aligned to the reference.

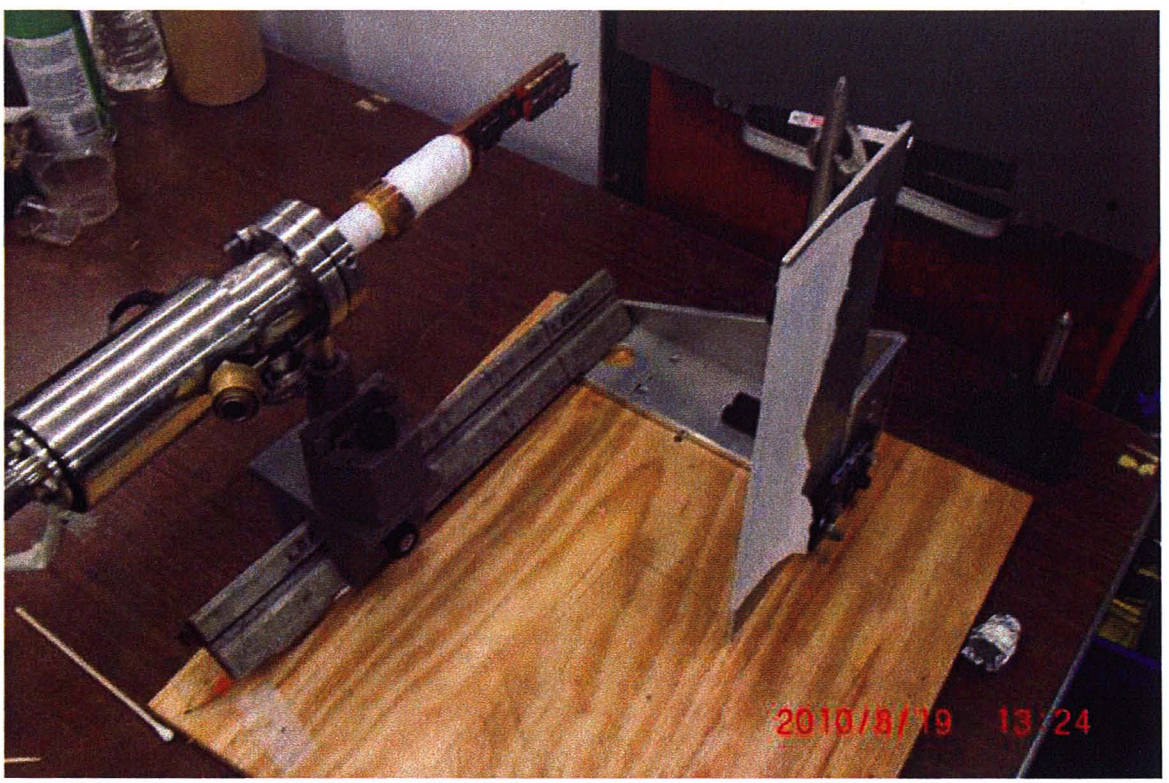

Figure 11: A view of the external alignment apparatus with the cryostat mounted

The brass cones are fitted with a set of two "anchor" screws on opposite ends. These holes are clearance holes and have threaded receptacles on the copper sample mount. When these screws are tightened, the head of the screw applies a downward pressure on the particular corner of the cone. On one end, a second set of "set" screws are added. These set screws are threaded on the cone and have no receptacle on the copper mount. These screws thereby apply an upward force on the brass cone when tightened. By alternating between applying downward torque with the anchor screws and upward torque using the set screws, a deflection of between 10 and 15 degrees is obtainable. In this manner, the laser spot reflected off each of the samples can be adjusted until they lie

within the reflection of the reference mirror.

After the samples are roughly aligned in the external alignment, the cryostat can then be mounted in its proper position next to the Bruker. With one of the visible light sources on, the light can be focused onto the sample using the concave incident mirror ('L1' on Figure 3). The cryostat should be cycled through each sample position to make sure the incident light spot is consistent in its coverage of each surface. The light is then collected on a second concave collection mirror ('L2' on Figure 3). With the appropriate detector mounted for the light used (generally MCT detector for its relative simplicity), the signal can then be maximized on the detector.

Lastly is the vertical optimization process which is repeated throughout the experiment as the temperature changes. In this process, the spectrum is monitored over a vertical distance of several millimeters above and below the sample position. A simple Gaussian-like behavior is observed in the signal intensity, which is then plotted and maximized for its optimal position. This process is done for each sample

2.3.5 In Situ Evaporation

The differences in size and surface geometry further complicate the measurement. Although the stainless steel is considered flat, it is rare in practice to grow a crystal without any surface imperfections or impurities. A technique called in situ evaporation is therefore used to coat the surface of the sample with a very thin layer of a highly reflective material (Homes et al., 1993). The thin layer fills any cracks and covers any

impurities to produce a highly reflective surface. In most spectral regions, gold is used for its near unity reflection properties. In the UV region, gold is not highly reflective, and so aluminum evaporation is performed.

Tungsten wire of thickness 0.015' is sanded, cleaned, and then wrapped into coils of 1 cm length. Then, a small amount of gold wire is tied to the coils in disconnected knots. The knots of gold wire must be disconnected to prevent electrical shortage of the current through the gold. When sufficient current is passed through the tungsten (roughly 12 Amps), the filament glows to and the gold melts. When performed under vacuum, the gold is ejected from the filament and pursues an outward trajectory until it comes into contact with a surface. Since there are three sample positions, it is necessary to have three unique coils prepared in the exact same manner to ensure an even layer of gold on each sample. The filaments are mounted onto a stainless steel plate, carefully insulated from electrical ground by use of peripholite washers (machined in the lab). The collimators are constructed out of brass and are also insulated electrically so that any unintentional contact between the coils and the collimator does not produce a short circuit.

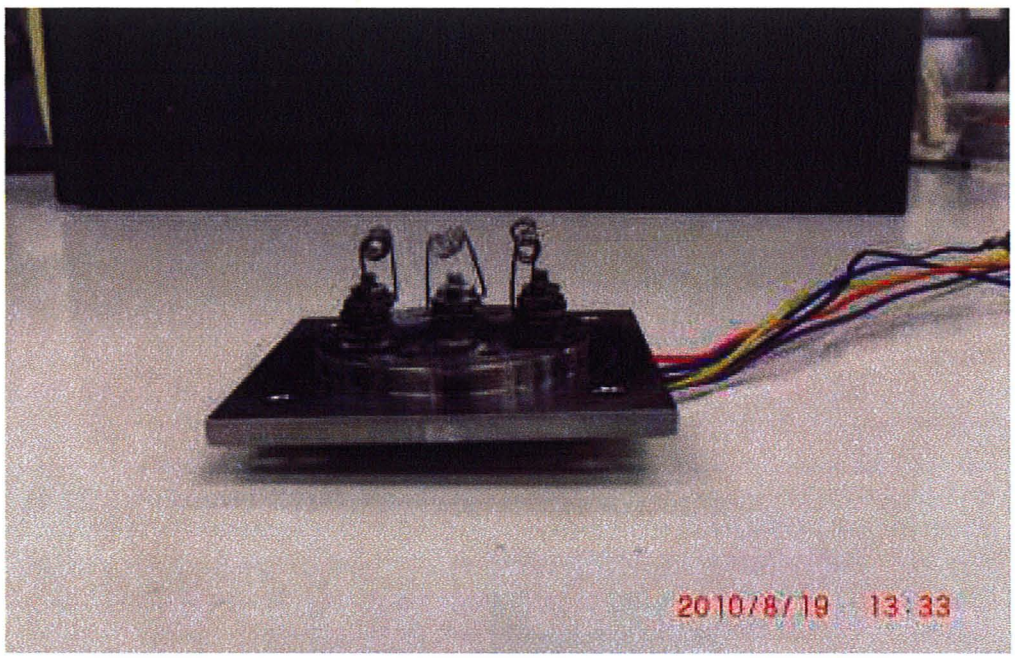

Figure 12: A side view of the evaporator plate, with three coils mounted

The final absolute reflectance is then constructed using a ratio of the form,

$$R_{sam}^{abs} = \left(\frac{R_{sam} / R_{ref}}{R_{coat}^{Au} / R_{ref}} \right) x R_{Au}^{abs}$$

In this ratio, the effect of the gold (or aluminum) coating is canceled by multiplying by the known reflectance of gold.

2.3.6 Temperature-dependency

The temperature of the sample is controlled by a Heli-tran open cycle cryogenic refrigeration system (or cryostat) produced by Advanced Research Systems, Inc. The

cooling is accomplished by the controlled transfer of liquid helium through a high-efficiency flexible transfer line to a heat exchanger. A small needle valve used in conjunction with an adjustable flow meter allows precise control of the flow rate, and thus better temperature stability. It was discovered that the speed of flow of helium created a torque on the transfer line that produced optical instability of up to 10%. For this reason, the pressure and rate of flow must be kept constant by use of a bubble flow gauge connected to the cryostat.

Since the samples are mounted directly to the thermal cold point of the cryostat, there is a significant thermal contraction effect that occurs throughout the experiment. Given the known length the copper sample mount and the coefficient of thermal expansion, the copper mount will contract by no more than 1 millimeter. However, a millimeter contraction is extremely large when compared to the wavelengths of light used and therefore must be accounted for experimentally. Although this information provides an estimate of the contraction between two given temperatures, it was found through practice that the best way to account was to repeat the vertical optical optimization process described above at each temperature.

2.3.7 Thermometry

Reliable and accurate temperature sensing is extremely crucial to the experiment, particularly at low temperatures where data is often required directly above and below the transition temperature. A Silicon diode thermometer is placed directly behind the sample

mounts. The diode is reliable to temperatures as low as 1.5 K, provided it is in good thermal contact. The thermal grounding of the connecting wires is also important so they are placed within a groove and sealed with silver tape.

In an effort to quantify the accuracy of the thermometry, the thermal reflectance of the heavy fermion system URu_2Si_2 (or URS) was measured. Although not to be discussed in great detail in this thesis, the URS system has a well-defined hidden-order transition temperature of T = 17.5 K, which is visible to us as a closing of a gap structure in the thermal reflectance. Thermal reflectance as a measurement technique will be described in greater detail in Section 5. As it relates here, the size of the gap observed at each temperature can be compared to the known transition temperature to gain an estimate in the degree of accuracy of our temperature readings.

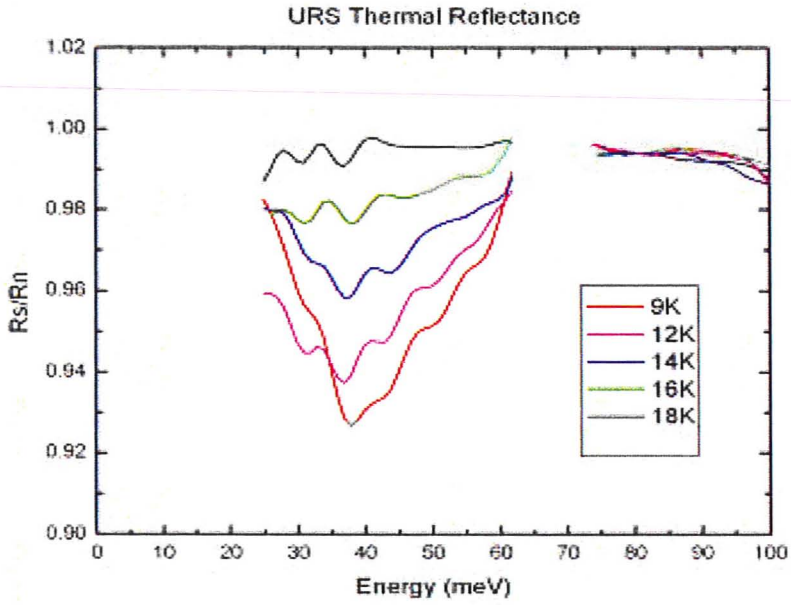

Figure 13: Thermal reflectance of URS, showing temperature dependence in the hidden order structure

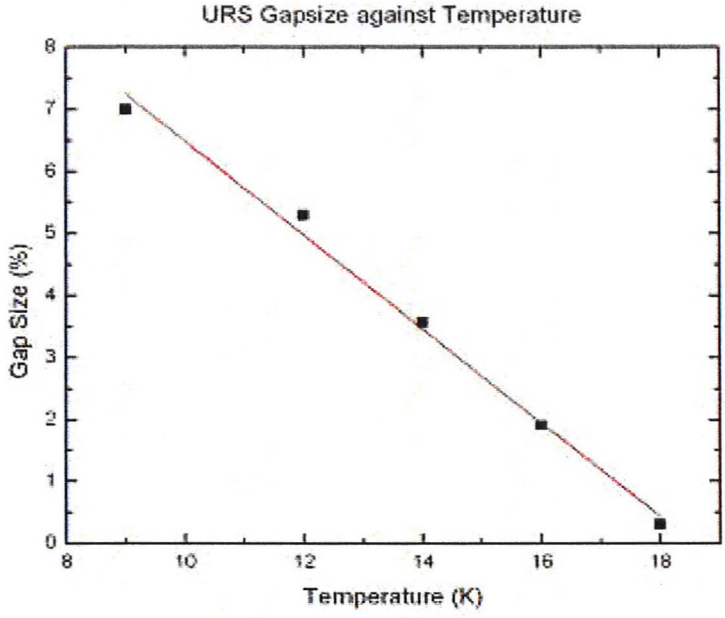

Figure 14: Size of the gap structure vs. temperature, showing an extrapolation to zero gap at T=18.2K

The graphs in Figure 13 and Figure 14 display a complete closing of the gap structure at T=18.2 K, suggesting the accuracy in our thermometry is to within 0.7 K. It is worth noting here that the vacancies shown in the data in Figure 13 are caused by beam splitter minimums and represent regions of poor quality data. This data is generally excluded from our analysis.

2.3.8 Reference mirror

It is not satisfactory for out measurements to be taken solely on the sample in question and instead requires a careful measurement of a pre-appointed reference. The

reference provides unique information on how the light source and the detector properties have changed throughout the measurement process. The reference is chosen for its weak temperature dependence, and therefore becomes a baseline for how our system is behaving. For our purposes, a highly polished piece of flat stainless steel is used as the reference mirror since stainless steel has very little absorption characteristics. By comparing the reflected spectrum of the sample to that of the steel reference, the specific qualities of the sample can be isolated. Changes in intensity of the detector/source are observed on the reference material and then are divided out of the final sample spectrum. These changes are bound to occur as the light sources are far from perfect in stability, and are bound to have degradation in time.

3. Theory and Analysis

3.1 Maxwell Formulation

Starting from Maxwell's equations for a material with a dielectric constant ε, conductivity σ, magnetic permeability μ, and speed of light c (Kittell, 1976):

$$\nabla \bullet H = 0$$

$$\nabla \bullet E = 0$$

$$\nabla x H = \frac{\varepsilon}{c}\frac{\delta E}{\delta t} + \frac{4\pi\sigma}{c}E$$

$$\nabla \times E = -\frac{\mu}{c}\frac{\partial H}{\partial t}$$

$$-\nabla^2 H = -\frac{\mu\varepsilon}{c^2}\frac{\partial^2 H}{\partial t^2} - \frac{4\pi\mu\sigma}{c^2}\frac{\partial H}{\partial t}$$

$$-\nabla^2 E = -\frac{\mu\varepsilon}{c^2}\frac{\partial^2 E}{\partial t^2} - \frac{4\pi\sigma\mu}{c^2}\frac{\partial E}{\partial t}$$

Taking the curl of the first set of equations yields second-order differential equations (second set) that are solvable with solutions of the plane wave form. Substituting this solution into the differential equation and setting the magnetic permeability to 1 reveals the complex index of refraction for a non-magnetic medium, N, as a function of frequency ω,

$$N \equiv \sqrt{\left(\varepsilon + i\frac{4\pi\sigma}{\omega}\right)} \equiv \eta + i\kappa$$

from which the real and imaginary dielectric function also follows,

$$\varepsilon_1 = \eta^2 - \kappa^2$$

$$\varepsilon_2 = 2\eta\kappa$$

As it relates to this study, plane wave solutions to Maxwell's equations are incident on a reflective metallic surface, and the incident and reflected field vectors E and B can be summarized as,

$$E_i + E_r = E_t$$

$$\frac{1}{\mu_i} B_i - \frac{1}{\mu_r} B_r = \frac{1}{\mu_t} B_t$$

where the subscripts denote the incident ('*i*'), reflected ('*r*'), and tangential ('*t*') components. Knowing $\eta = \frac{c}{v}$ and $|E| = \frac{v}{c}|B|$, these equations are combined to yield a ratio of the reflected field over the incident field in terms of the refractive indices. This reflectance ratio, *r*, is of particular importance to reflectance spectroscopy.

$$r = \frac{E_r}{E_i} = \frac{\eta_i - \eta_t}{\eta_i + \eta_t}$$

For our purposes, the incident medium is vacuum so $\eta_i = 1$. Electric fields are observed in the real world as intensity, it is more relevant to refine a reflection coefficient of $R = r\,x\,r^*$,

$$rr^* = R = \frac{(1-\eta)^2 + \kappa^2}{(1+\eta)^2 + \kappa^2}$$

Now, defining the reflected wave vector as a complex function, the real and imaginary

components of the index of refraction can be written in terms of R and complex phase θ,

$$\eta = \frac{1-R}{1+R-2\sqrt{R}\cos(\theta)}$$

$$\kappa = \frac{-2\sqrt{R}\sin\theta}{1+R-2\sqrt{R}\cos(\theta)}$$

The quantity R is the reflection measured by our technique, and the phase is then calculated using a method called the Kramers-Kronig analysis

3.2 Kramers-Kronig analysis.

The Kramers-Kronig analysis is a mathematical formulation based on the relationship between the real and imaginary part of a complex function. The process involves an application of Cauchy's residue theorem for integration of complex functions, and is relevant for any complex function that is analytic (that is, locally convergent) in the positive plane. For any complex function, the real and imaginary components are related by their principle Cauchy integrals,

$$\alpha_1(\omega) = \frac{2}{\pi} P \int_0^\infty \frac{s\alpha_2(s)}{s^2-\omega^2} ds$$

$$\alpha_2(\omega) = -\frac{2\omega}{\pi} P \int_0^\infty \frac{\alpha_1(s)}{s^2-\omega^2} ds$$

where the subscripts 1 and 2 denote the real and imaginary components of an arbitrary complex function, respectively. The Kramers-Kronig formulation is of particular relevance to optical spectroscopy as it can be used to determine the complex phase of the

reflectivity, given a measured R.

$$\theta(\omega) = \frac{\omega}{\pi} \int_0^\infty \frac{\ln R(\omega') - \ln R(\omega)}{\omega^2 - \omega'^2} d\omega'$$

3.3 Dielectric function and the Drude model

One important result of applying the Kramers-Kronig formulation to optical systems is the discovery of the optical sum rule and it's correspondingly defined plasma frequency ω_p,

$$\int_0^\infty \sigma(\omega) d\omega = \frac{\omega_p^2}{8}$$

$$\omega_p^2 = \frac{4\pi N e^2}{m}$$

With these definitions, it is possible to arrive at an expression for the dielectric function written as a summation of the contributions by high-frequency interband oscillators (using the index k),

$$\varepsilon(\omega) = 1 + \omega_p^2 \sum_k f_{k,o} \left(\frac{1}{\omega_\kappa^{\,2} - \omega^2} + i \frac{\pi}{2\omega_k} \partial(\omega_k - \omega) \right)$$

The Drude model was proposed in 1900 by Paul Drude to explain simply the transport of charge and electrons through the surface of a metal by treating the electrons as solid mass with a finite scattering rate within a kinetic model framework. In the Drude model, electron-electron and electron-ion interactions are ignored. It is therefore prudent to calculate the dielectric contribution of a metal conforming to the Drude model with a Lorentzian peak. Using the generalized dielectric function above, it can be found to be,

$$\varepsilon(\omega) = 1 + \frac{4\pi N e^2}{m} \frac{1}{{\omega_k}^2 - \omega^2 - i\omega\Gamma}$$

where Γ is the width of the Lorentzian peak. This can be generalized a series of n oscillators,

$$\varepsilon(\omega) = 1 + \sum_k^n \frac{{\omega_{pk}}^2}{{\omega_k}^2 - \omega^2 - i\omega\Gamma}$$

This formula can then be used to describe the dielectric function of any quantum mechanical system. The most relevant application is for a simple Drude metal, with the only scattering occurring at zero frequency. For this simple model, the dielectric function becomes,

$$\varepsilon(\omega) = \varepsilon_\infty + \frac{{\omega_D}^2}{-\omega^2 - i\omega\Gamma}$$

where the subscript D represents the Drude component. This can then be compared to the dispersion relation for this system,

$$q^2 = \frac{\omega^2}{c^2}\left(\varepsilon_\infty + i\frac{4\pi\sigma}{\omega}\right)$$

to arrive at the conductivity of a Drude metal defined in terms of a scattering rate $1/\tau$.

$$4\pi\sigma_D = \frac{{\omega_D}^2}{1/\tau - i\omega}$$

The real and imaginary conductivity of this Drude model is illustrated graphically in Figure 15.

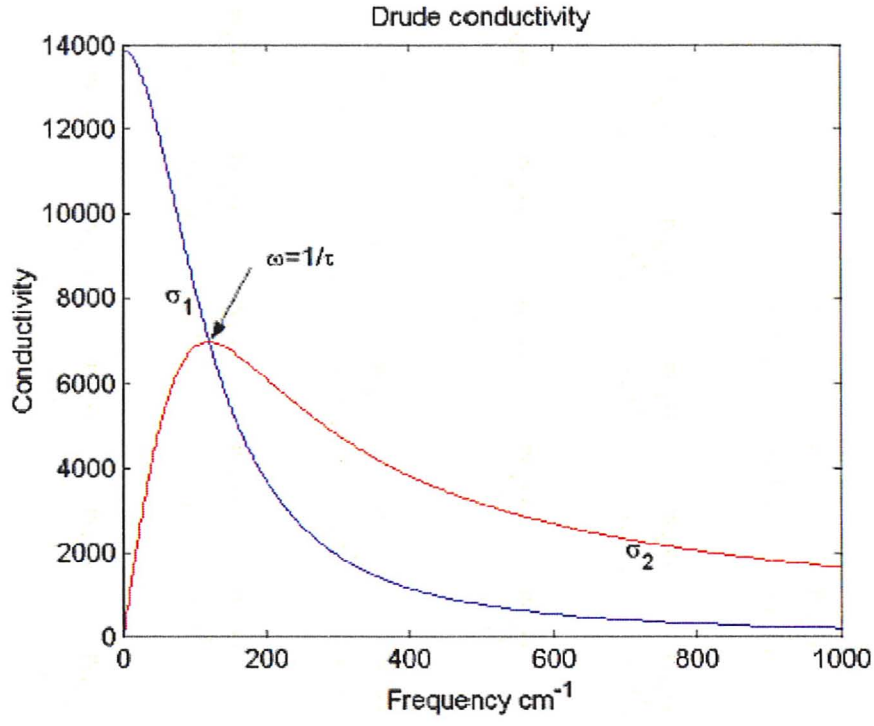

Figure 15: Illustration of the real and imaginary components of the Drude conductivity

In this simple model, the scattering rate is considered a static quantity as only elastic scattering of electrons from lattice defects are considered.

This formulation requires careful consideration in regions where the frequency is much lower than the $1/\tau$. In this low frequency region, the behaves according to the Hagen-Rubens approximation,

$$1-R=\sqrt{\frac{\omega}{2\pi\sigma}}$$

This formula is a low frequency approximation of the reflectance of a Drude metal where the electrons are scattered by static defects.

3.4 Extended Drude model

Although this model is adequate for very simple metals, it requires an expansion to describe more realistic materials. In the extended Drude model, the scattering rate $1/\tau$ is assumed to frequency dependence instead of a static value. Substituting this change into previously described conductivity yields,

$$4\pi\sigma(\omega) = \frac{{\omega_p}^2}{1/\tau - i\omega} = \frac{{\omega_p}^2}{1/\tau(\omega) - i\omega[1+\lambda(\omega)]}$$

Or

$$4\pi\sigma(\omega) = \frac{{\omega^*}_p^{\,2}(\omega)}{1/\tau^*(\omega) - i\omega}$$

Where $1/\tau^*(\omega)$ denotes a mass renormalized quantity. Here then, the frequency-dependent scattering rate can be written as,

$$1/\tau(\omega) = \frac{{\omega_p}^2}{4\pi}\mathrm{Re}\left(\frac{1}{\sigma(\omega)}\right)$$

This provides a direct link between the measured complex conductivity, $\tilde{\sigma}(\omega) = \sigma_1(\omega) + i\sigma_2(\omega)$, and the scattering rate. It is clear that the value of plasma frequency is crucial to the analysis. For our purposes, the plasma frequency can be determined by an integration of the real part of the conductivity in the low frequency regime.

$$\omega_p = \sqrt{\frac{120}{\pi}\int_0^{\omega_c}\sigma_1(\omega')d\omega'}$$

The integration stretches from the zero frequency limit up to a defined "cutoff frequency", ω_c. This cutoff frequency denotes the end of the Drude component of the conductivity, and can be determined from a minimum in the frequency-dependant absorption curves in a technique described by J. Hwang. The method requires the identification of the low frequency Drude absorption peak, where the minimum between the Drude absorption and higher frequency bands defines the cutoff frequency (Hwang et al., 2007).

The scattering rate becomes critical to the analysis of the so called Bosonic Spectral function. The spectral function, $I^2\chi(\omega)$, provides information on the bosons responsible for the frequency dependence of the scattering rate. In our analysis, the spectral function is uncovered by the use of a technique pioneered by Ewald Schachinger and Jules Carbotte called the Maximum Entropy Inversion. This method starts with a deconvolution of the optical scattering rate,

$$\frac{1}{\tau_{op}(\omega,T)} = \int_0^\infty d\Omega K(\omega,\Omega;T) I^2\chi(\Omega)$$

Here T is the temperature of the system, and $K(\omega,\Omega;T)$ is a mathematical kernel. For the purposes of the High-temperature superconductors with d-wave symmetry, the kernel is written (Schachinger, Neuber, and Carbotte, 2006).

$$K(\omega,\Omega;T=0) = \frac{2\pi}{\omega}\left\langle (\omega-\Omega)\theta(\omega+2\Delta_0(\vartheta)-\Omega)E\left(\sqrt{1-\frac{4{\Delta_0}^2(\vartheta)}{(\omega-\Omega)^2}}\right)\right\rangle_\vartheta$$

where $\Delta_0(\vartheta) = \Delta_0\cos(2\vartheta)$ is the size of the d-wave gap.

The Maximum Entropy Inversion method is used in this thesis (Schachinger et al., 2006), although it is not common to all spectroscopy groups. Other groups have different techniques for uncovering the spectral function, and the validity of our method will be explored in the next chapter.

4. Proof of concept of Maximum Entropy Inversion

4.1 Introduction

One piece of crucial information that can be gained from an optical study is the bosonic spectral function as a function of frequency and temperature. As the temperature decreases from the normal state into the superconducting state, a change in the spectral function may yield crucial information on the underlying mechanisms responsible for the onset of superconductivity. It has been proposed by J. Hwang in years previous that a shift in boson frequency is observed in optimally doped Bi-2212 (T_c = 96 K), an observation not expected of a strict electron-phonon interaction. At temperatures well below the transition, a sharp boson peak is observed at 55 meV, a gap structure is seen from 100-150 meV, and a broad background is observed at higher energies. As temperature is raised, the primary sharp beak at 55 meV is weakened, and slightly broadened, but the gap and background structure remains. It is only above the transition temperature that this gap begins to close, at T = 100 K. At increasingly higher temperatures, the sharp peak is seen to broaden substantially, and shifted in frequency to 80 meV. At room temperature, the spectrum is dominated by a simple broad background peak. These observations are summarized in Figure 16, taken from the original paper by J. Hwang. (Hwang, 2006)

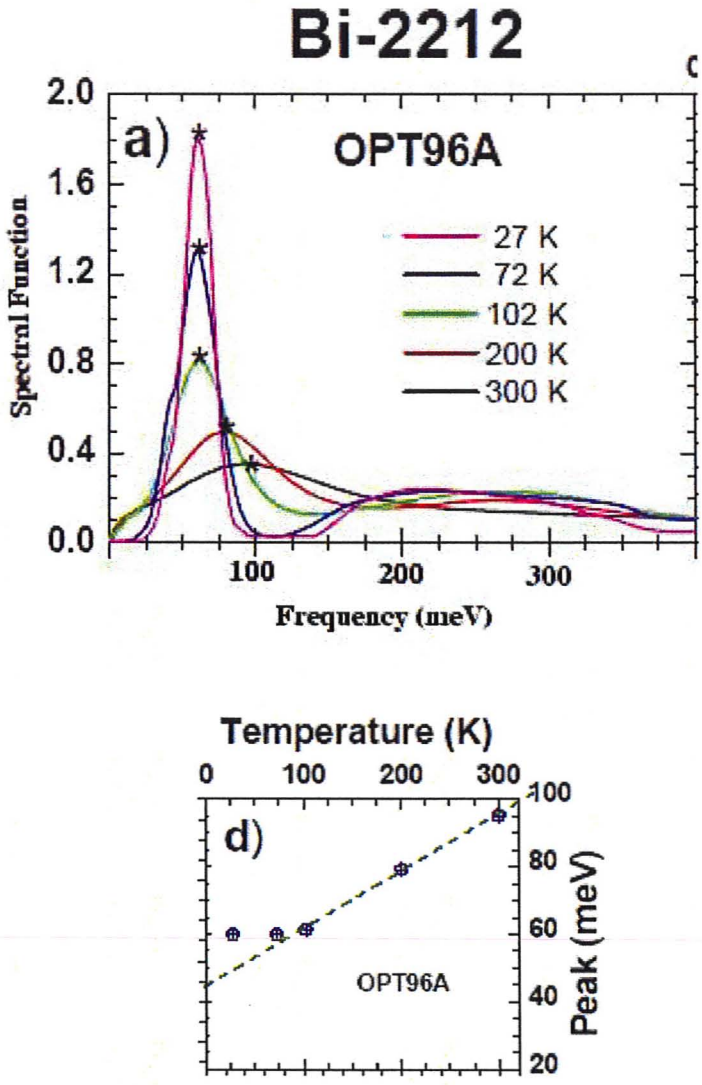

Figure 16: Published results by Hwang et al. of the bosonic spectral function for the Bi-2212 superconductor. The top shows the observed spectral function, and the bottom image shows the dependence of position peak on temperature. Note the peak shifts in frequency.

It is clear from these two graphs that there is a 20 meV shift between 100 K and 200 K, and an additional 20 meV shift up to room temperature. This observation has been contested by competing optics groups who have proposed that this may be an artifact of

our Maximum Entropy inversion technique described earlier (van Heumen, 2008).

It is therefore necessary to illustrate the effectiveness of our technique in identifying a spectral function that evolves with temperature. By use of the Shulga extension of the Allen formula, a variety of synthetic spectral functions were employed to generate a "test" reflectances at all temperatures. These reflectances were then processed by the KK and Maximum Entropy techniques to reveal the underlying bosonic spectral function.

The inversion process allows for the input of a sigma variance parameter. This sigma value is a statistical approach to the fitting process and establishes a lower limit for the deviation of the fitted curve to the dataset. In practice, this value is first allowed to be large and then all subsequent inversions involve decreasing values of sigma, thereby creating a tighter fit to the data. The tightness of the fitting parameter increases the iteration count required for the software to find an appropriate fit, and is limited by the quality of the data. Applying a sigma that is too small will cause an error when the program fails to converge to a solution. Decreasing the sigma variance can also introduce noise in the inverted spectrum as the software is able to respond to much smaller changes in the data.

4.2 Thermal Broadening

This first relevant question is to quantify the effect of unavoidable thermal broadening. The inversion process can only be accurate to the resolution limited by the

thermal energy of the system. Naturally, lower temperatures contain less thermal broadening. This requires quantification, and to study this effect, reflectances from two sharp peaks (40 meV and 80 meV) fixed in frequency and width were generated at a series of temperatures and the resolution of the inversion method was tested. The results of the inversion process are shown in Figure 17, and the height of the minimum is plotted in Figure 18.

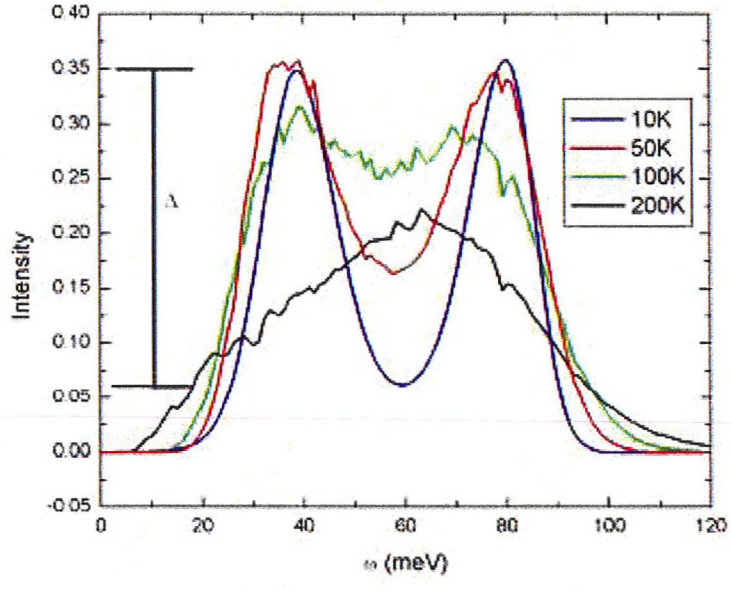

Figure 17: Bosonic spectral function extracted by the Maximum Entropy Inversion method from synthetic reflectance at various temperatures. The synthetic spectrum contains a peak at 40 meV and 80 meV. Low temperature results show the two peaks sharply, while higher temperatures contain more noise and thermal broadening until the resolution of the peaks is lost at 200 K. Here, sigma variance $\sigma = 0.3$.

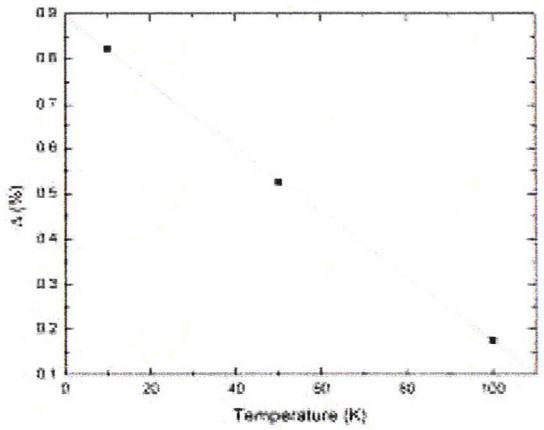

Figure 18: Size of the minimum between the two peaks as a function of temperature, showing the loss of resolution of the two peaks with increasing temperature.

There is a clear and unmistakable smearing with temperature on the order of 2kT as shown on figure 17. The synthetic function was replicated with both peaks and widths matching to within 1%. As the temperature rises, the minimum in intensity between the two peaks begins to wash out although the peak locations themselves show very little evolution. At 100 K we are approaching the breaking point for where we can no longer resolve the two peaks. However the Rayleigh criterion of the gap is still satisfied at this temperature. The Rayleigh criterion is a generally accepted criterion for the resolution of two nearby images, which is just satisfied when the maximum diffraction of one image (or peak) coincides with the minimum diffraction limit of the second. It is also worth noting that the location of the two peaks is unchanged through this low temperature regime. It is only when we approach 200 K that the thermal smearing becomes too large to resolve the peaks on this energy scale. Figure 18 shows the intensity between the two

peaks at different temperatures.

4.3 Biased inversion

The software used for the inversion process contains options for the temperature, the error tolerance, and most importantly an option to "bias" the inversion results in favor of lower temperatures. In the biased scheme, the inversion is first performed at very low temperatures to obtain an inverted spectrum. This inverted spectrum is then used to bias the results of the inversion at higher temperatures. The biasing program initially assumes a solution identical to that of the low temperature result, and then adjusts slightly to fit the input data. It is important to our understanding of the inversion process to investigate the effects of this biased inversion scheme.

To begin, a reflectance is generated at low temperatures using an input spectral function of a single peak located at 36 meV. To truly understand the effect of biasing, it is important to know whether or not a temperature evolution of peak location is resolvable under both biased and unbiased mode. For this reason, the 36 meV is shifted up to 39.5 meV at 100 K, and to 43.5 meV at 200 K (10% shift for each). The resulting scattering rate was inverted using the Maximum Entropy inversion technique, and the result of the unbiased mode is shown in Figure 19.

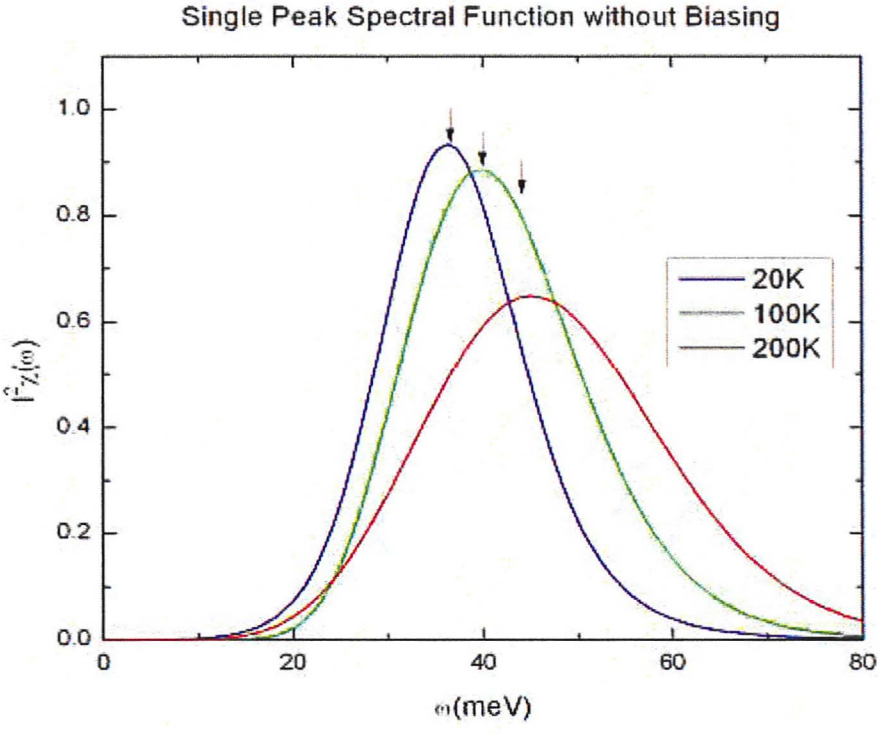

Figure 19: Single peak spectral function as inverted by the Maximum Entropy inversion method, showing a clear shift with increasing temperature. The arrows denote the positions of the peaks used to generate the 1/tau spectra. The agreement between the synthetic structure and the inverted spectra is excellent. Here, $\sigma = 0.5$.

The unbiased mode clearly shows an evolution of the peak location with temperature, along with some of the thermal broadening discussed earlier. It is worth noting that the smoothness of the high-temperature data shown here is quite pronounced when compared to Figure 17, and this is a result of a larger sigma variance used here (0.5 was used here, as opposed to 0.3 in Figure 17). The quantification of these shifts will be tabulated below.

The next step is to test the strength of the biased inversion process. The process is

repeated using the same datasets, however this time the spectra will be biased towards the lower temperature results. Since 20 K is the lowest temperature available here, it is unchanged between the two modes. The effect of the biasing on the higher temperatures is shown here,

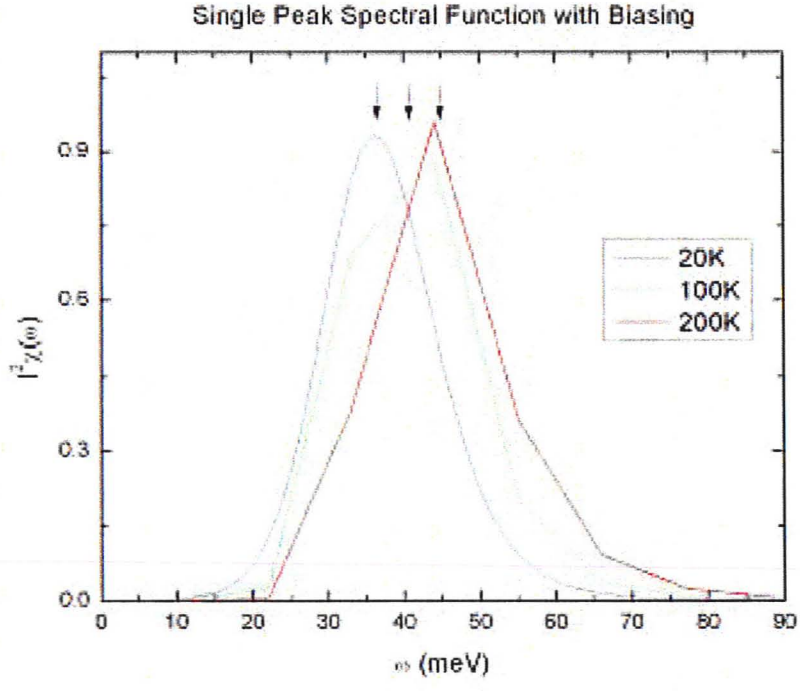

Figure 20: Single peak spectral function under biased inversion. The temperature evolution is still present here, although the quality of the data suffers. Once again, the arrows denote the precise location of the peak in the synthetic spectrum. The variance used is $\sigma = 0.5$.

It is clear that the inversion under biased mode does indeed show the desired temperature evolution, although it is also clear that the quality of the inverted data takes a significant loss. The location of the peaks for both the biased and unbiased mode along

with the expected value as generated are summarized in table 2.

T	Synthetic Peak Location (meV)	Shift from 10 K (meV)	Unbiased Maximum Entropy Inversion (meV)	Measured Shift (meV)	Biased Maximum Entropy Inversion (meV)	Measured Shift (meV)
10 K	36.5	0	36.5	0	36.5	0
100 K	40.15	3.65	39.9	3.4	39.5	3
200 K	44.16	7.66	45	8.5	43.4	6.9

Table 2: Peak locations as found by inversion along with the expected values. A peak at 36.5 meV at 10 K is allowed to shift by 3.65 meV and 7.66 meV at 100 K and 200 K respectively. Both the unbiased and biased inversions detect the shift but with a loss of accuracy at increasing temperature.

At its worst, the inversion is shown to be accurate to within 2% of the input function. At low and intermediate temperatures, it is our conclusion that the unbiased mode allows for closer replication of the desired input single peak function. This is also apparent in qualitative terms as the curves in figure 19 appear a lot smoother than those shown in figure 20.

As an extension to this investigation, the synthetic spectral function is now expanded to a two-peak system. As a result of preliminary investigations, the ability of the biased mode to identify the temperature dependency of a two peak structure has been called into question. For this test, a spectrum is generated at T = 20 K with sharp peaks at 36 meV and 112 meV, and a second spectrum is generated at T = 100 K with peaks at 36 meV and 123 meV (second peak shifted up in frequency by 10%). It is important to know whether the conclusion reached on the single peak structure can be verified with the two

peak structure. The uncovered spectrum under unbiased mode is shown graphically in Figure 21.

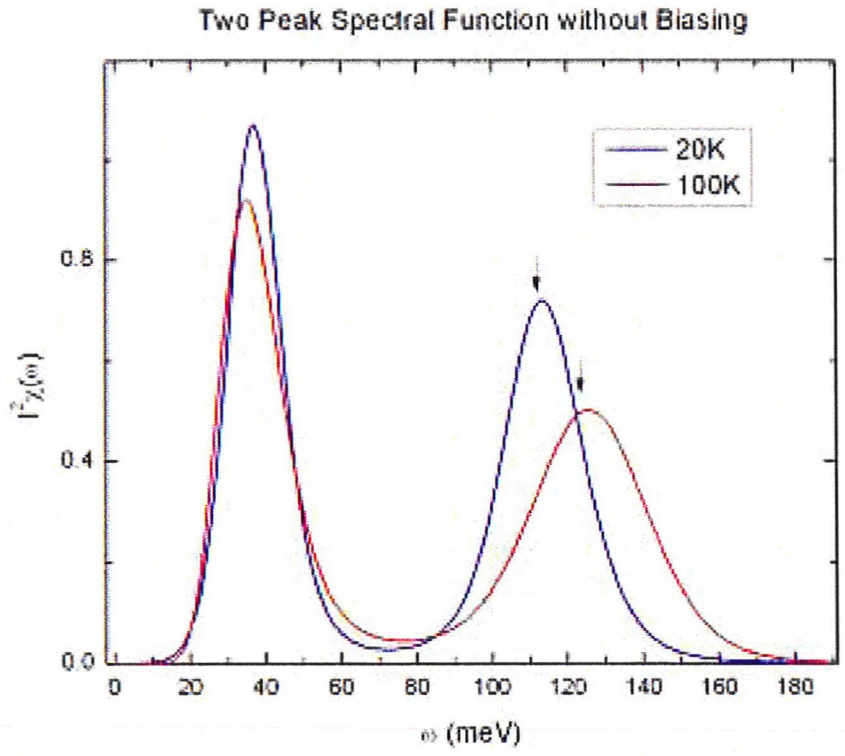

Figure 21: Unbiased inversion from a synthetic two peak spectral function, showing a clear evolution with temperature. The second peak been shifted to 123 meV in the synthetic spectrum, although the inversion process suggests a shift of 125.4 meV. Once again, $\sigma = 0.5$.

All results of the two peak structure are quantified in table 3 below. The designed shift in the spectral function was very clearly replicated, to an accuracy of 0.7%. As before, the process is repeated using a biasing system that uses low temperature results as a preferred solution. The biased curves also display the degradation in data quality seen in figure 21, but show a similar conclusion,

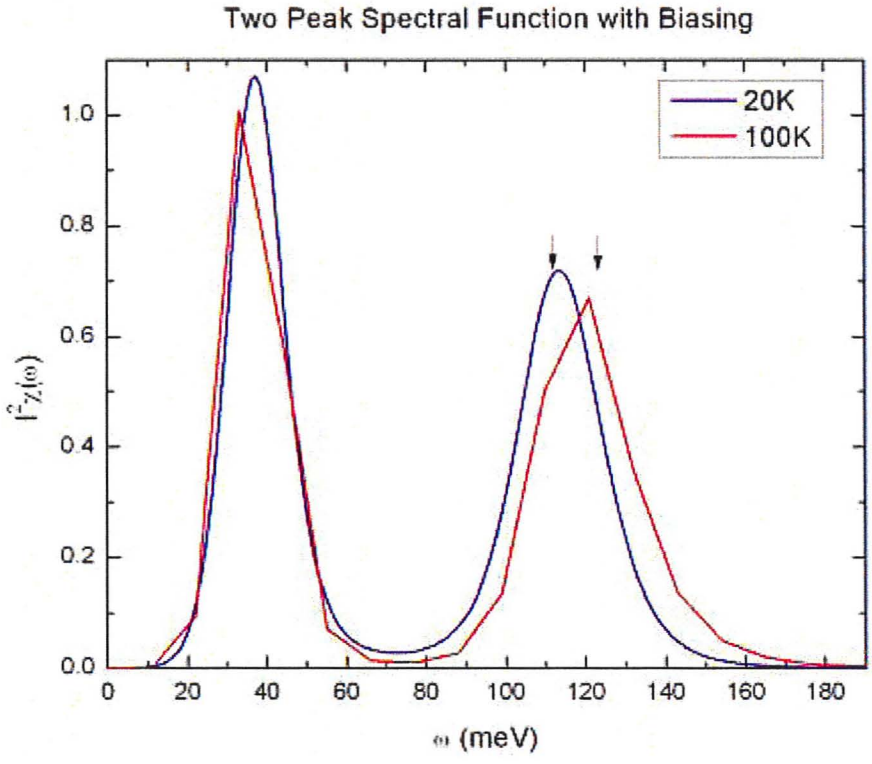

Figure 22: Biased inversion of figure 21. The decrease in data quality is inherent in the biased inversion process. The second peak is synthetically located at 123 meV, although it is seen here at 118.5 meV. Sigma variance is unchanged, $\sigma = 0.5$.

The result of the bias mode inversion also shows a shift, although it can be seen that the shift shown here is less than that in figure 21. More precisely, the shift in the biased mode inversion is 3.7% lower than the expected value of 123 meV, while the unbiased mode is 1.9% above the expected value. The results of these graphs are tabulated in table 3.

T	Synthetic "second" Peak Location	Maximum Entropy Peak Location	Deviation from expected
20 K	112 meV	112.8 meV	0.8 meV (0.7%)
100 K	123 meV	125.36 meV	2.36 meV (1.9%)
100 K biased	123 meV	118.5 meV	4.5 meV (3.7%)

Table 3: Second peak locations as found by Maximum Entropy inversion along with the expected values. The biased mode shows more discrepancy between the expected peak location and the inverted peak location.

Although both the biased and the unbiased mode are able to provide the correct qualitative behavior, the unbiased mode provides inverted spectra that are closer to their expected values, and is therefore preferable. For the remainder of this thesis, unbiased inversion mode is used exclusively.

4.4 Bi-2212

Of particular importance to our group is to test the validity of the Maximum Entropy inversion method used in the Bi-2212 paper, and to show that thermal broadening from the inversion technique does not account for all of the results seen in Figure 16. A competing optics group led by E. van Heumen also measured the Bi-2212 material and did not observe the same evolution in the spectral function (van Heumen, 2008). If van Heumen is correct, thermal broadening in the inversions at higher

temperature using the same synthetic function would account for all of the results seen in Figure 16. If the peak is seen in the same location at all temperatures, then the shift reported by Hwang et al. is a result of underlying mechanisms and not an artifact of our technique. To study this, the Shulga extension to the Eliashberg theory was used to create a fixed synthetic spectral function with a sharp peak at low energies and broad background at higher frequencies. The synthetic spectrum is unchanged between temperatures. The reflectance is calculated, and then the inversion process is performed independently. The result of this inversion process is illustrated below

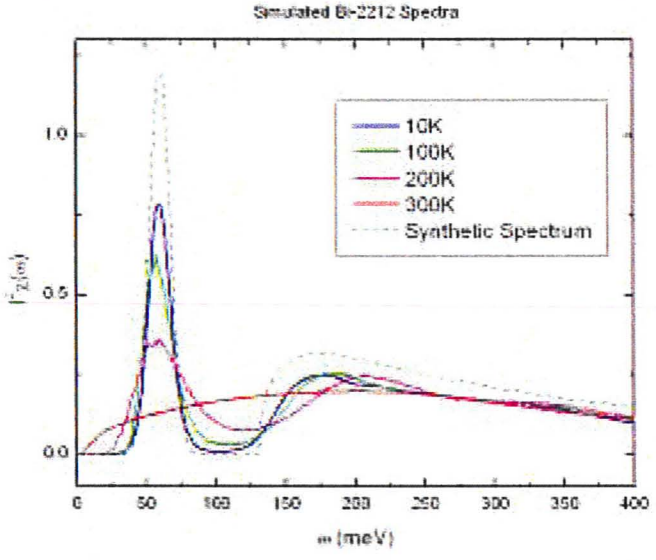

Figure 23: A temperature independent input spectral function inverted at successively higher temperatures. The location of the first peak is unchanged up to temperatures as high as 200K, albeit with a small amount of thermal smearing. The dashed line represents the original synthetic spectrum that was used to generate $1/\tau$. The agreement in frequency dependency is striking.

The plot above shows some of the unavoidable "blurring" of the results as higher temperatures are reached but the thermal widening of the both the sharp peak and the broad background peak does not effectively close the gap completely. More notably, however, is that the location of this sharp peak is unchanged with pure thermal effects. From this we can conclude that the evolution in peak position shown in figure 16 is not strictly an artifact of the thermal broadening, but instead is a result of a physical process in the material. Superimposed over the results from the Bi-2212, the conclusion is more obvious (Figure 24). From this, we conclude that that the shift of boson frequency observed in Bi-2212 cannot be explained by simple thermal broadening, and instead a product of the underlying physics of the system. It is clear that intermediate temperatures contain a low energy peak that shifts to higher energies when outside of the superconducting region.

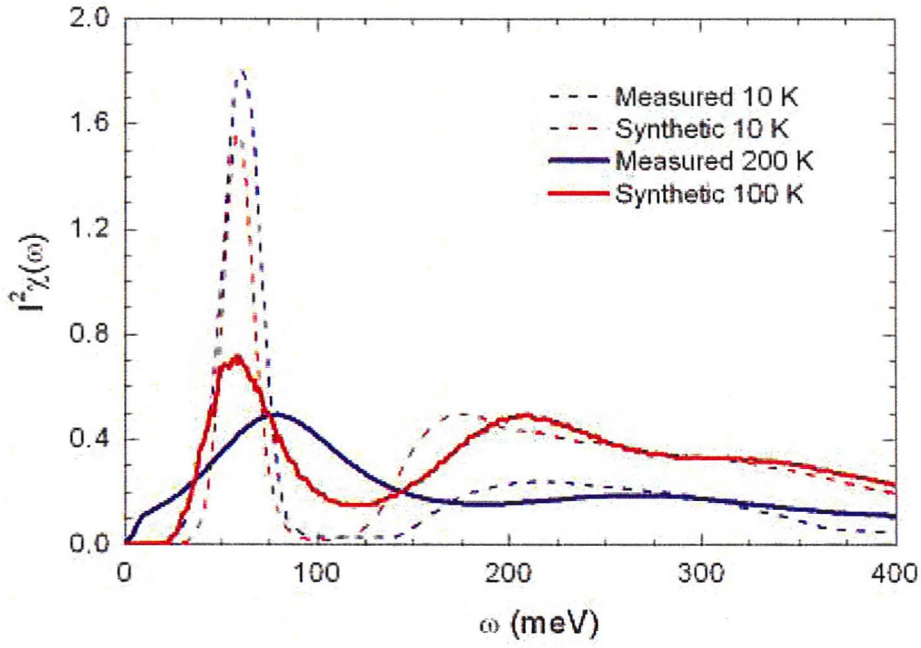

Figure 24: A comparison of the synthetic spectral function data set (red) at T = 20 K and T = 200 K temperatures against the inverted spectral function from the experimental data of the Bi-2212 sample (blue) at the same temperatures. Both sets show a smearing between the peak and the background at intermediate temperatures, although the synthetic data does not display the shift in the first peak's location. Through this analysis, we can conclude the shift seen in the experimental data is real and a result of underlying physics, and not simply an artifact of the inversion.

5. BaFeCoAs Results

5.1 Introduction

After the experimental apparatus was constructed, it then becomes prudent to test the quality of the measurement. For this purpose, the iron pnictide superconductor BaFeCoAs was selected for its availability. The sample has the chemical formula of $BaFe_{1.8}Co_{0.2}As_2$ and transition temperature of T = 22 K.

5.2 Growth

The $BaFe_{1.8}Co_{0.2}As_2$ crystals (6 were received) were grown by Athena Sefat at Oak Ridge National Laboratory using the self-flux method. The crystals themselves are roughly 2 mm by 2 mm in size, and can be cleaved to reveal a highly lustrous surface. On inspection, very little surface defects are observed. The samples are hygroscopic, and therefore require storage in a desiccator when not under vacuum.

5.3 Thermal Reflectance

One of the early tests on the $BaFe_{1.8}Co_{0.2}As_2$ involved the measurement of the thermal reflection of the sample. This allows us an immediate observation of the strength of particular sample as a superconductor, as well as providing us an immediate result to be compared to the preliminary results of other optics groups on the same material. The thermal reflectance is simply the ratio of the reflectance below the superconducting transition over the one taken above the transition temperature. The transition temperature

of $BaFe_{1.8}Co_{0.2}As_2$ is T = 22 K and our calculation of the thermal contraction of our apparatus levels off at these temperatures. For this reason, measurements can be done without any changes in the optimized cryostat position.

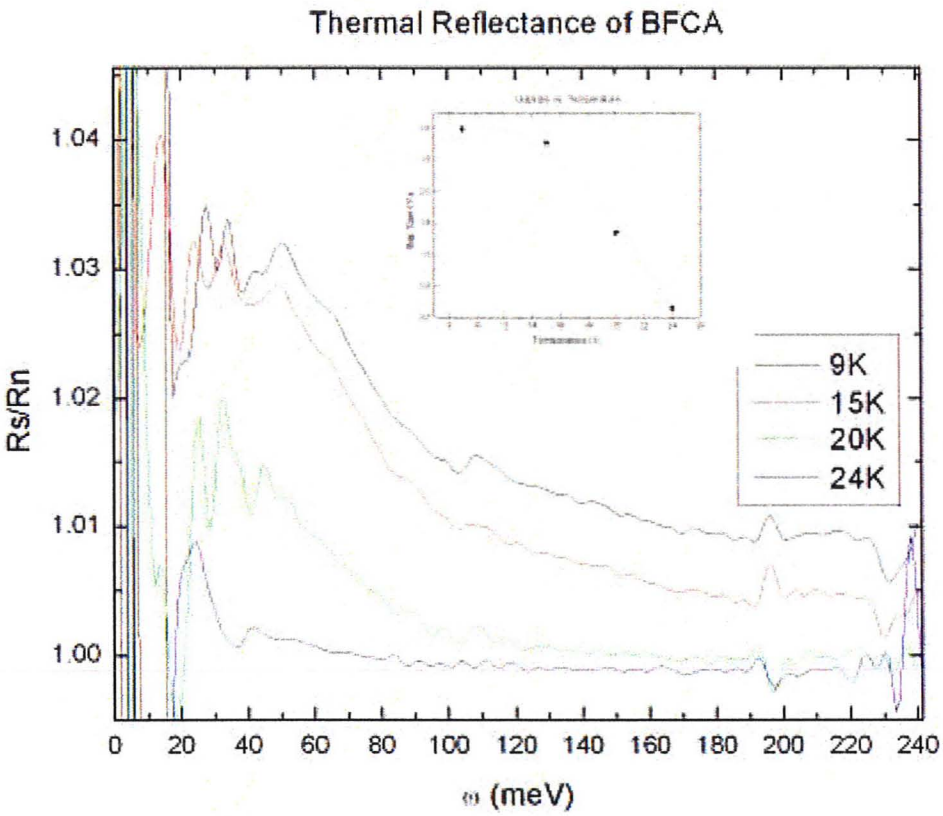

Figure 25: Thermal reflectance (superconducting reflectance over normal state reflectance) of the $BaFe_{1.8}Co_{0.2}As_2$ sample illustrating the increase in reflectance in the superconducting state. At 9 K, the reflectance is enhanced up to 3%, a clear signature of superconductivity. The inset shows the amplitude of the gap structure as a function of temperature.

The results are shown here in Figure 25 and show a ratio in the reflectance of the sample between the superconducting state and the normal state. The peak-like structure

represents the decreased absorption strength of the superconducting state at very low energies, a signature of the superconducting gap. The strength of this superconducting gap is understandably dependent on temperature. The reflectance at 40 meV can be plotted against temperature to yield a superconducting order parameter, plotted in the inset of Figure 25. This parameter goes to zero at T ~ 24.1 K which signifies the closing of the gap structure and the emergence of the normal state properties.

5.4 Absolute Reflectance

The next step of our measurement is to measure the absolute reflectance spectra at all relevant temperatures using the *in situ* gold evaporation method described in section 2.3.5. The *ab* plane reflectance is measured using the Bruker apparatus at energies ranging from 50 cm^{-1} to 40,000 cm^{-1} at temperatures from 15 K to 300 K. The experiment is split into 5 components corresponding to a particular frequency range (Table 1). Figure 26 shows the absolute reflectance on $BaFe_{1.8}Co_{0.2}As_2$ as measured. The low energy behavior of the data as a function of temperature shows an increase in reflectance as the temperature is decreased which is expected for a metal as lower temperatures causes the sample to become increasingly metallic, and therefore more reflective.

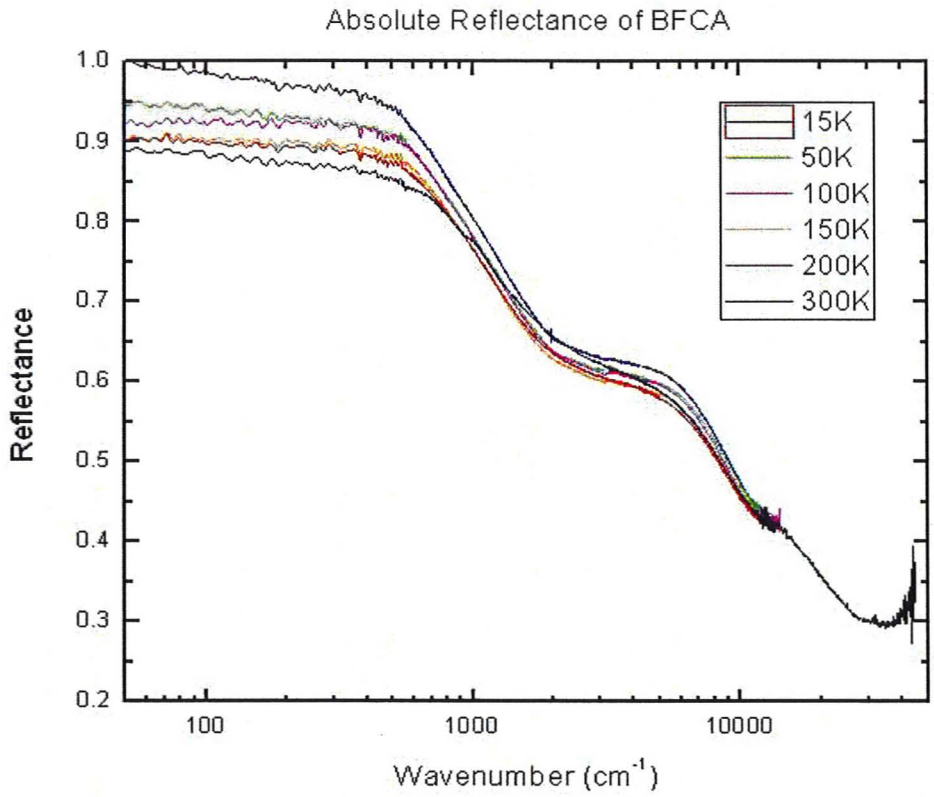

Figure 26: Absolute reflectance shown over all spectral regions. In general terms, the low energy reflectance increases as the temperature drops which is a signature of the sample becoming more metallic. The reflectance suggests a plasma edge of 265 meV (2139 cm^{-1}).

It is worth noting that the value of reflectance at $\omega = 50$ cm^{-1} is 0.88 at 300 K, a value that is unexpectedly low. Other groups (Wu et al., 2009) have observed a reflectance at room temperature as high as 0.96 in this region. The quality of the crystal used in our experiment could be responsible for some of the decreased reflectance, although a more likely scenario is an unexpected change in the sample position during the actual measurement process. This calls for further investigation.

As described in the theory section, analysis of this reflectance can yield many important quantities relevant to the study of transport properties in this material. The measured reflectance is converted to an optical conductivity through Kramers-Kronig analysis. The Kramers-Kronig (section 3.2) analysis requires integration from zero to infinity so extrapolations beyond our data at low and high frequencies are required for the data analysis. At low energies below the range of our measurement, the material is assumed to exhibit metallic conductivity as dictated by the Hagen-Rubens approximation (where 1-R varies as square root of frequency). In the high energy regime above the maximum frequency of the data, the reflectance is extrapolated as ω^{-1} up to 1E6 cm^{-1}. Above this frequency, the material is assumed to exhibit free electron behavior, and is therefore extrapolated as ω^{-4}. Figure 27 displays the optical conductivity (real component) for this material.

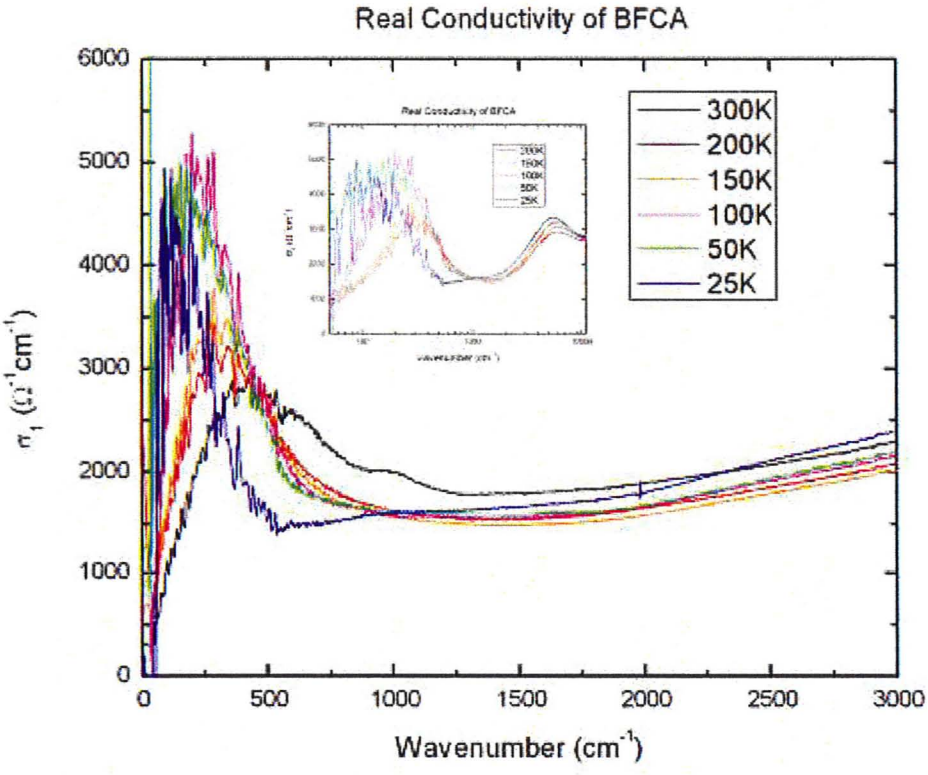

Figure 27: Real component of the optical conductivity (inset displays log-scale of the same data). At low energies, the scattering of free electrons as predicted by the Drude model is displayed as in upturn in conductivity at the low end of our data. However, an anomalous behavior is seen below 50 cm^{-1} in that a pure Drude component would extrapolate linearly to a DC conductivity value. In our analysis, the conductivity is seen to rapidly decay as zero frequency is approached. This is likely a result of poor measurement at these energies. At higher energies, the conductivity contains a broad peak at 5500 cm^{-1}. This peak does not display temperature dependence.

For a Drude metal, the conductivity should increase as frequency decreases until it saturates and levels to a constant value, a feature not seen here. This anomaly is intrinsically connected to the discrepancy in the reflectance values at low frequencies, and is likely caused by a change in sample position during the experiment. This warrants

a repetition of the experiment with emphasis on the low energy regime. This decay of conductivity in our sample is not seen by other optics groups such as Wu et al. (Section 5.5). The conductivity also displays a temperature independent absorption peak absorption at 5500 cm^{-1}, a feature that is seen in Wu's experiment.

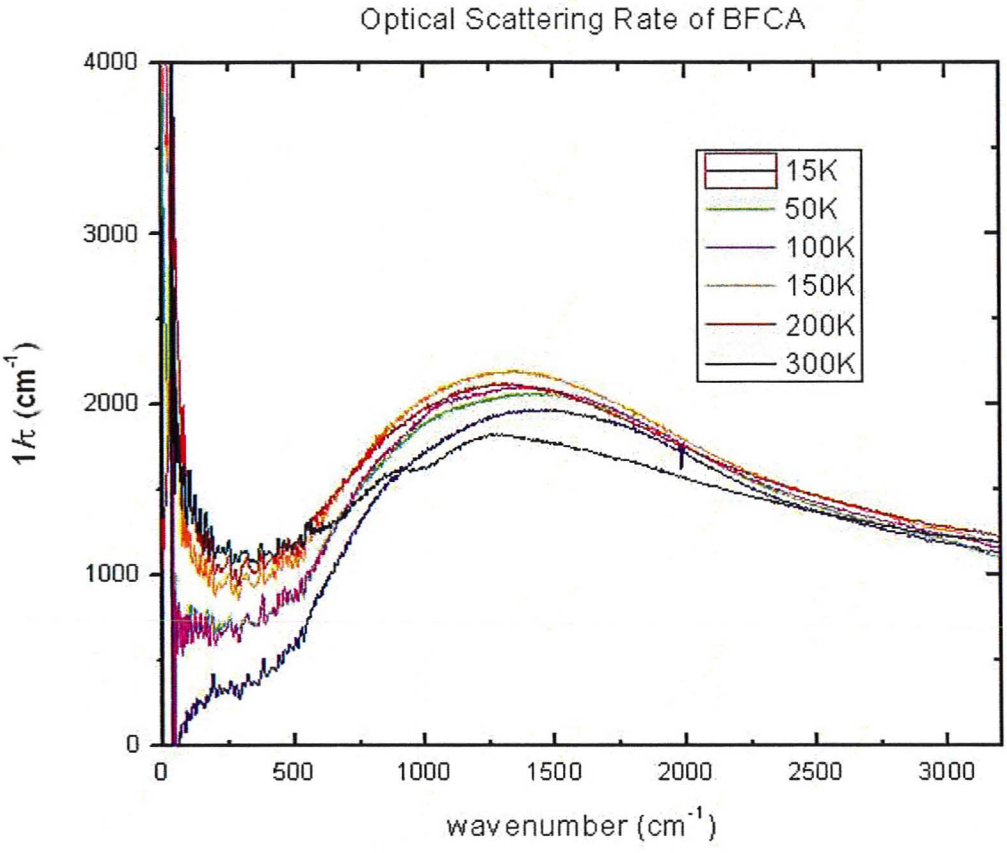

Figure 28: Optical scattering rate shown at low energies. The scattering found at very low frequency represents impurity scattering. At low temperatures, high frequency excitations are not expected. There is an apparent onset of scattering at low temperatures at 520 cm^{-1}.

In addition to the conductivity shown, the frequency-dependent optical scattering rate was also calculated. To calculate the optical scattering rate, a plasma frequency

ω_p introduced in section 3.3 and 3.4 needs to be found. The plasma frequency can be determined by an integration of the real part of the conductivity in the low frequency regime. Here, the plasma frequency is calculated to be 14,400 cm^{-1}. Figure 28 shows our results for measured scattering rate below 3000 cm^{-1} for the six temperature values using this plasma frequency. The scattering displays the characteristic behavior of an increase in scattering at low frequency with increasing temperature. The most clearly defined curve, the 15 K curve, shows a gap structure at 6.5 meV that is closed at 50 K. There is evidence of residual elastic scattering on order of 250 cm^{-1} at low frequency, which yields a residual resistivity of 76 $\mu\Omega$ cm, a reasonable value for this material. The rapid onset in scattering at 500 cm^{-1} indicates the presence of a boson at this frequency. The 300 K is anomalous in that its background scattering is lower than that of the low temperature data. This is likely an artifact of poor data quality at room temperature, and should not be interpreted physically.

The Maximum Entropy Inversion method (Schachinger, 2006) was then performed on the low temperature scattering rate. The sigma variance was chosen to be large initially, and lowered on successive iterations until a tight fit to the input data is achieved. Here, a final sigma value of 0.3 was attainable. The inversion was done under unbiased mode in accordance with the findings reported in Chapter 4. The data used in the inversion is shown in Figure 28, and no smoothing filters were applied. Figure 29 shows the bosonic spectral function recovered under these conditions. The inversion process was performed using the "normal state" inversion technique, a limitation of the

current software.

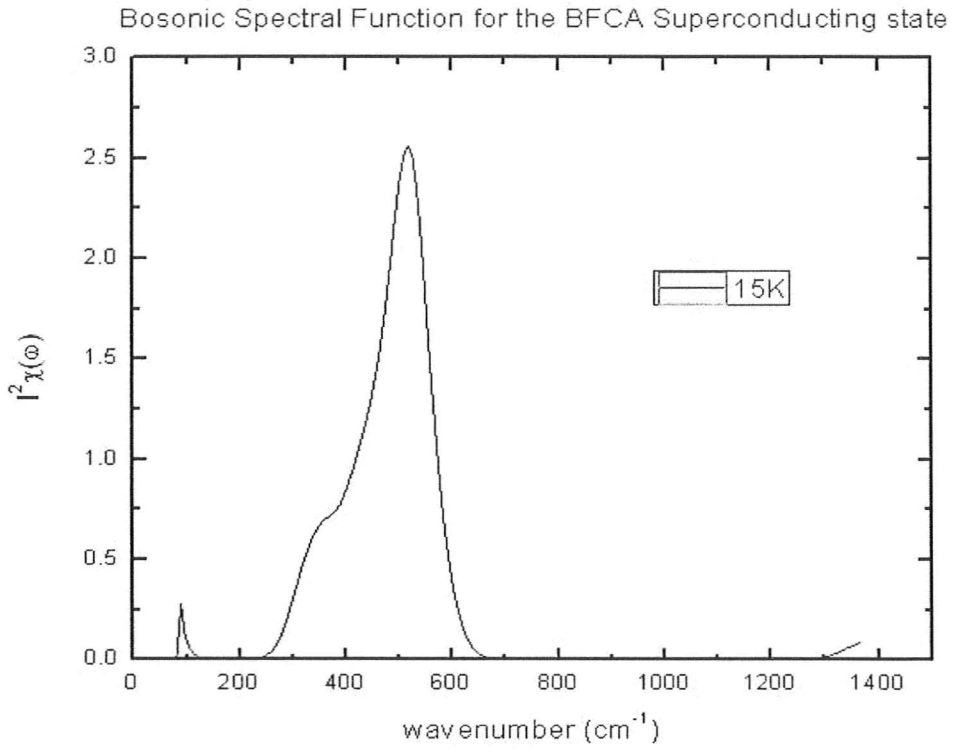

Figure 29: Bosonic spectral function of the superconducting state showing a sharp boson peak at 518 cm^{-1} at 15 K. The feature seen at 100 cm^{-1} (outside of the peak structure) is artifacts of the inversion are not to be interpreted physically. This plot suggests the presence of a bosonic interaction at 64 meV and can be seen to correspond to a sharp increase in scattering rate shown in Figure 28. For this inversion, a sigma variance of $\sigma = 0.3$ was used.

The spectral function shows a well-defined peak at 518 cm^{-1} (or 64 meV) along with a very small "hump" like feature at 375 cm^{-1} (46 meV). Higher temperature inversions did not prove successful, and are therefore excluded from this thesis. It is likely that the quantity of noise in the data limits the success rate of the inversion, and is more

problematic as the thermal noise is increased at higher temperatures. In future work, successful inversions at higher temperature are expected. Then, information can be gathered on the evolution of the bosonic peak as the sample leaves the superconducting region and insight on the underlying mechanism responsible for the transition can be obtained.

An additional piece of information can be gained from performing an integration of the spectral function over all frequencies to obtain a mass renormalization factor. The integration takes the form,

$$\lambda = 2\int_0^\infty d\Omega \frac{I^2 \chi(\Omega)}{\Omega}$$

The spectrum obtained in Figure 29 is integrated to find a renormalization parameter of 4.04 at 15 K. This is comparable to renormalization parameter found at low temperatures on a related superconductor ($Ba_{0.55}K_{0.45}Fe_2As_2$) measured by J. Yang (Yang et al, 2008) in previous experiments. Yang reported $\lambda = 3.42$ at T = 28 K which evolved to 0.79 at ambient temperatures. Future work will likely yield bosonic spectral features at higher temperatures, and thereby a direct comparison of the temperature dependence will be possible.

5.5 Comparison to other data

To get an idea on the reproducibility of our data, it is prudent to compare to other competing optics groups that have performed these measurements on this material. It

should be noted that the samples were grown independently and could then have slightly different doping levels and impurities. Figure 30 is the previously shown real component of the optical conductivity on a log-scale to emphasize the low energy regime. This conductivity can be compared to the results of D. Wu et al. (Wu et al., 2009) (Figure 31).

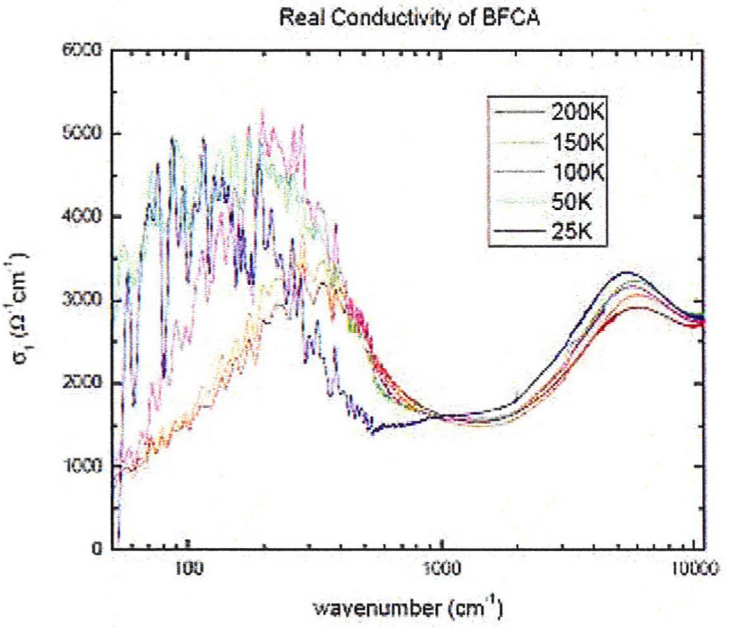

Figure 30: Real conductivity on log scale emphasizing the low frequency features. The non-Drude decay of conductivity below 50 cm^{-1} and is likely a measurement artifact.

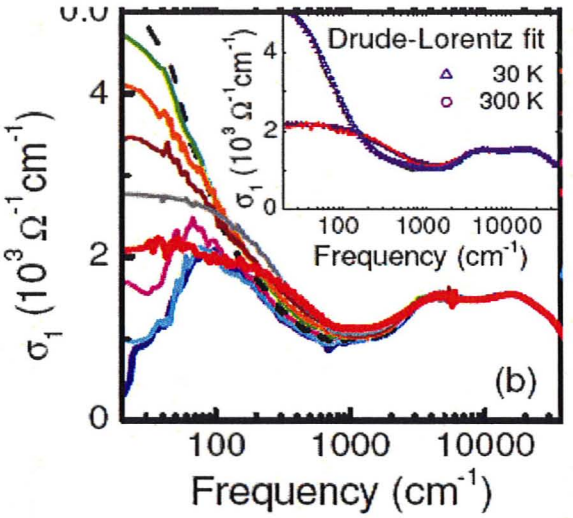

Figure 31: Optical conductivity of $BaFe_{1.8}Co_{0.2}As_2$ as measured by D. Wu et al. The grey curve is at 200 K, and the black dashed line is at 30 K.

At 100 cm^{-1}, Wu reports a conductivity of 2800 ohms^{-1} cm^{-1} at 200 K (grey curve), while we observe only 1750 ohms^{-1} cm^{-1}. The agreement is slightly better at low temperatures (30 K) where Wu reports 3000 ohms^{-1} cm^{-1} and we see 3700 ohms^{-1} cm^{-1}. The two conductivities both display an interband absorption at 5500 cm^{-1} (or 681 meV). As the temperature is decreased, a Drude-like contribution develops and becomes narrower in Wu's data. Wu's results at zero frequency do not exhibit the decay of conductivity that we observe below 100 cm^{-1}. Our data contains a considerable amount of noise here, and it is an ongoing exercise to improve the data quality. Wu et al. did not calculate the bosonic spectral function, so no direct comparisons can be made.

6. Conclusions

In conclusion, the thesis presented here represents progression towards a stable and reliable optical spectroscopy apparatus, although the reliability of the recent results has significant room for improvement. The new experimental design has many conceivable advantages over the previous design, and significant progress has been made towards optical stability with the new apparatus. These advantages include achieving lower temperatures than previously, and the opportunity to measure multiple samples in a single experiment. Developments in the reproducibility of the data include an external alignment device and an optimization technique that can function at all temperatures. Studies on the thermal reflectance of $BaFe_{1.8}Co_{0.2}As_2$ have proven successful, although the measurement is simple in that it requires no sample movement. The absolute reflectance measurement has had varying degrees of success, and further work is required to provide reliable results at all temperatures.

An investigation into the Maximum Entropy Inversion method of uncovering the bosonic spectral function has been performed in an effort to confirm a conclusion by Hwang et al. (Hwang et al., 2006) in a superconducting Bi-2212 sample. Hwang et al. reported a shift in boson peak location to higher frequencies as the temperature rises above the superconducting transition. This conclusion has been contested by competing optics groups who suggest that the evolution seen is purely an artifact of the inversion technique, and does not correspond to underlying physics (van Heumen, 2008). In initial tests, the effect of thermal broadening on the spectra is revealed to be on the order 2kT.

Beyond thermal effects, the inversion method includes an option to "bias" higher temperature inversions using the low-temperature spectrum as a trial solution. There was an initial concern that this biasing can effectively force the higher temperature spectrum to mimic that of low temperature. If this were to be true, then the ability to identify bosonic evolution is lost completely. To investigate this, both a single-peak and a double-peak synthetic spectra were generated, both of which contain a designed frequency shift of 10% per temperature step. The spectra were then inverted using both the biased and the unbiased scheme. As summarized in chapter 4, the biased mode does indeed recognize the shift (in both single and double peaks), but the magnitude of the shift varies slightly from the expected 10%. The unbiased mode also shows the shift, although the magnitudes in this scheme are more closely linked to the expected value. Lastly, a synthetic spectrum that is very similar to the Bi-2212 at low temperature was generated with no temperature evolution. If the shift reported by Hwang et al. would be visible in the synthetic inversions then the criticism of our technique is correct. However, the spectra show no shift of peak position, as displayed in figure 23. The conclusion is that the shift observed by Hwang et al. is a result of underlying physical mechanisms, and not simply an artifact of the inversion technique.

Results in this thesis include both thermal and absolute reflectance as observed on $BaFe_{1.8}Co_{0.2}As_2$, as well as some pertinent optical constants derived from this reflectance. Shown are the relevant graphs for the complex conductivity, as well as the optical scattering rate. The optical scattering rate shows a small gap-like structure at low energies

for temperatures below the transition, although the resolution of this gap is not ideal. The low temperature data has been inverted using the technique described in chapter with modest success. A peak in the bosonic spectrum is identified at 64 meV. Higher temperature inversions were not feasible due to the quality of the data. The data is shown to have qualitative similarities to that of a measurement performed by D. Wu et al., which suggests that our apparatus is indeed uncovering the correct physical processes, although with less than ideal resolution. An anomalous behavior is seen in our data at very low energies where the conductivity appears to decay rapidly as opposed to leveling to a constant value (as described by Drude). This will require a repetition of the experiment to confirm or disprove the low energy decrease in conductivity.

Further work will continue on this study in the near future. Ongoing efforts to improve the optical stability of the apparatus are continuing. Once the data can be measured to a better accuracy, the inversion process will be performed on all temperatures to attempt to detect any evolution of the boson peaks. Additionally, the study will be extended to include BaFeCoAs of different doping in order to quantify the boson shifts as it relates to chemical composition.

7. References

Bardeen, J., Cooper, L., and Schrieffer, J.R. (1957). *Phys. Rev.,* 108, 1175.

Basov, D.N. and Timusk, T. (2005). *Rev. Mod. Phys.,* 77, 721.

Bednorz, J.G. and Mueller, K.A. (1986). *Z. Phys. B*, 64, 189.

Carbotte, J.P. (1990). *Rev. Mod. Phys.,* 62, 1027.

Carbotte, J.P. and Schachinger, E. (2006). *Ann. Phys.,* 15, 585.

Farnworth, B. and Timusk, T. (1976). *Phys. Rev. B*, 14, 5119.

van Heumen, E., et al. (2008). arXiv:0807.1730v3 [cond-mat.supr-con]

Homes, C.C., Reedyk, M.A., Crandles, D.A., and Timusk, T. (1993). *Appl. Opt.,* 32, 2976.

Hwang, J., Timusk, T., and Gu, G.D. (2007). *J. Phys.: Condens. Matter,* 19, 125208.

Hwang, J., et al., arXiv:cond-mat/0607653v2 [cond-mat.supr-con]

Kittel, C. (1976). *Introduction to Solid State Physics.* John Wiley and Sons Inc., New York, 5th edition.

Onnes, H.K. (1911). *Commun. Phys. Lab. Univ. Leiden*, 12, 120.

Schachinger, E., Neuber, D., and Carbotte, J.P. (2006). *Phys. Rev. B,* 73, 184507.

Wu, D., et al. (2009). arXiv:0912.3334v2 [cond-mat.supr-con]

Yang, J., et al., (2008). arXiv:0807.1040v1 [cond-mat.supr-con]